

# JGR Solid Earth

## RESEARCH ARTICLE

10.1029/2022JB025302

### Special Section:

Advances in understanding volcanic processes

### Key Points:

- Tephra blanket of the 2021 Tajogaite eruption is only 7%–16% of the total volume but is key to decipher the variable eruptive dynamics
- Tephra blanket shows distinct layers and units at different distances from vents that well correlate with tremor and lava emission rate
- Hybrid eruptions are best described based on both event duration and mass associated with multiple products (tephra blanket, cone, lava)

### Supporting Information:

Supporting Information may be found in the online version of this article.

### Correspondence to:

C. Bonadonna,  
Costanza.Bonadonna@unige.ch

### Citation:

Bonadonna, C., Pistolesi, M., Biass, S., Voloschina, M., Romero, J., Coppola, D., et al. (2022). Physical characterization of long-lasting hybrid eruptions: The 2021 Tajogaite eruption of Cumbre Vieja (La Palma, Canary Islands). *Journal of Geophysical Research: Solid Earth*, 127, e2022JB025302. <https://doi.org/10.1029/2022JB025302>

Received 1 AUG 2022

Accepted 7 NOV 2022




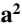






### Author Contributions:

**Conceptualization:** Costanza Bonadonna, Marco Pistolesi  
**Data curation:** Costanza Bonadonna, Marco Pistolesi, Sébastien Biass, Marija Voloschina, Jorge Romero, Diego Coppola, Arnau Folch, Luca D'Auria, Alba Martín-Lorenzo, Lucia Dominguez, Camille Pastore, Maria-Paz Reyes Hardy

© 2022. The Authors.

This is an open access article under the terms of the [Creative Commons Attribution-NonCommercial-NoDerivs License](https://creativecommons.org/licenses/by/4.0/), which permits use and distribution in any medium, provided the original work is properly cited, the use is non-commercial and no modifications or adaptations are made.

## Physical Characterization of Long-Lasting Hybrid Eruptions: The 2021 Tajogaite Eruption of Cumbre Vieja (La Palma, Canary Islands)

Costanza Bonadonna<sup>1</sup> , Marco Pistolesi<sup>2</sup> , Sébastien Biass<sup>1</sup> , Marija Voloschina<sup>2</sup> , Jorge Romero<sup>3</sup> , Diego Coppola<sup>4</sup> , Arnau Folch<sup>5</sup> , Luca D'Auria<sup>6,7</sup> , Alba Martín-Lorenzo<sup>6,7</sup> , Lucia Dominguez<sup>1</sup>, Camille Pastore<sup>1</sup>, Maria-Paz Reyes Hardy<sup>1</sup>, and Fátima Rodríguez<sup>6</sup> 

<sup>1</sup>Department of Earth Sciences, University of Geneva, Geneva, Switzerland, <sup>2</sup>Department of Earth Sciences, University of Pisa, Pisa, Italy, <sup>3</sup>Department of Earth and Environmental Sciences, University of Manchester, Manchester, UK, <sup>4</sup>Department of Earth Sciences, University of Torino, Torino, Italy, <sup>5</sup>Geosciences Barcelona (GEO3BCN-CSIC), Barcelona, Spain, <sup>6</sup>Instituto Volcanológico de Canarias (INVOLCAN), San Cristóbal de La Laguna, Tenerife, Canary Islands, <sup>7</sup>Instituto Tecnológico y de Energías Renovables (ITER), Granadilla de Abona, Tenerife, Canary Islands

**Abstract** Long-lasting, hybrid eruptions can be of complex description and classification, especially when associated with multiple eruptive styles and multiple products. The 2021 Tajogaite eruption of La Palma, Canary Islands, was associated with a magma-gas decoupled system that resulted in the simultaneous emission of lava flows and tephra plumes from various vents. Even though the tephra blanket ( $\sim 2 \times 10^7$  m<sup>3</sup>) represents only 7%–16% of the total erupted volume, it provides fundamental insights into the overall eruptive dynamics. Tephra was mostly dispersed NE-SW due to a complex regional and local wind patterns and was subdivided into 3 units and 11 layers that well correlate at different distances from the vent and with both tremor data and lava emission rate. While plume height varied at the temporal scale of a few hours, the average mass eruption rate associated with the tephra blanket of the different units remained relatively constant ( $\sim 3\text{--}4 \times 10^3$  kg s<sup>-1</sup>). In contrast, the emission rate of lava largely increased after the first week and remained higher than the overall emission of tephra throughout the whole eruption (average value of  $\sim 6 \times 10^4$  kg s<sup>-1</sup>). Based on a detailed characterization of the tephra blanket in combination with atmospheric wind, tremor, and lava emission trend, we demonstrate the need of (a) multidisciplinary strategies for the description of hybrid eruptions that account for both the duration of individual phases and the quantification of the mass of multiple products, and of (b) dedicated ash dispersal forecasting strategies that account for the frequent variations of eruptive and atmospheric conditions.

**Plain Language Summary** Volcanic eruptions are mostly subdivided into effusive and explosive when they are associated with the emission of lava flows or with the fragmentation of magma that results in the generation of widespread deposits (i.e., tephra). The September–December 2021 Tajogaite eruption of La Palma Island (Spain) represents a typical example of long-lasting, hybrid eruption with alternation, or, more often, contemporaneous emission of lava flows and tephra. The lava field extended toward the western sector of the island, while the tephra blanket was mostly dispersed NE-SW due to a complex regional and local wind pattern. Even though the tephra blanket represents only 7%–16% of the total erupted volume, it provides fundamental insights into the overall eruptive dynamics. Based on a detailed characterization of the tephra blanket, in combination with wind, seismic tremor, and lava emission trend, we demonstrate the need of dedicated strategies for the description of hybrid, long-lasting eruptions that account for both eruption duration and for the quantification of multiple products (tephra blanket, tephra cone, lava flows). We also show the need of dedicated strategies of short-range ash dispersal forecasting that account for the frequent variations of eruptive and atmospheric conditions.

## 1. Introduction

Volcanic eruptions are commonly subdivided into effusive and explosive activity depending on conduit dynamics that can either result in the outflow of lava when the degassed magma reaches the surface (effusive eruptions), or in the fragmentation of magma at various depths (dry explosive eruptions, from Hawaiian to Ultra-Plinian, and wet explosive eruptions from Surtseyan to phreato-Plinian in the classification of Walker (1980)). Nonetheless, some

**Formal analysis:** Costanza Bonadonna, Marco Pistolesi, Sébastien Biass, Marija Voloschina, Diego Coppola, Arnau Folch, Luca D'Auria

**Funding acquisition:** Costanza Bonadonna

**Investigation:** Costanza Bonadonna, Marco Pistolesi, Sébastien Biass, Jorge Romero, Diego Coppola, Arnau Folch, Luca D'Auria, Alba Martin-Lorenzo, Lucia Dominguez, Maria-Paz Reyes Hardy, Fátima Rodríguez

**Methodology:** Costanza Bonadonna, Marco Pistolesi, Sébastien Biass, Diego Coppola, Arnau Folch, Luca D'Auria

**Project Administration:** Costanza Bonadonna

**Resources:** Costanza Bonadonna, Marco Pistolesi, Diego Coppola, Arnau Folch, Luca D'Auria, Alba Martin-Lorenzo, Fátima Rodríguez

**Software:** Diego Coppola, Arnau Folch

**Supervision:** Costanza Bonadonna, Marco Pistolesi

**Visualization:** Costanza Bonadonna, Marco Pistolesi, Sébastien Biass, Marija Voloschina, Diego Coppola, Arnau Folch

**Writing – original draft:** Costanza Bonadonna, Marco Pistolesi, Marija Voloschina, Diego Coppola, Arnau Folch, Luca D'Auria

**Writing – review & editing:** Costanza Bonadonna, Marco Pistolesi, Sébastien Biass, Marija Voloschina, Jorge Romero, Diego Coppola, Arnau Folch, Luca D'Auria, Alba Martin-Lorenzo, Lucia Dominguez, Camille Pastore, Maria-Paz Reyes Hardy, Fátima Rodríguez

eruptions associated with both silica-poor (e.g., basalt) and silica-rich magma (e.g., rhyolite) can be associated with hybrid styles that include both effusive products (e.g., lava flows, lava domes) and explosive features (e.g., tephra blankets, scoria cones, pyroclastic density currents) resulting from variable eruptive styles (e.g., Alfano et al., 2018; Cassidy et al., 2018; Castro & Gardner, 2008; Pioli et al., 2009; Schipper et al., 2013; Wadsworth et al., 2020; Zawacki et al., 2019). In particular, long-lasting eruptions (durations from a few days to a few years) can be characterized by unsteady dynamics and simultaneous emission of lava and tephra; this can be the result of various processes including the shallow fragmentation of basaltic magma and episodic gas segregation, i.e., violent Strombolian eruptions (Cioni et al., 2008; Hill et al., 1998; Macdonald, 1972; Pioli et al., 2008, 2009; Valentine, 1998; Valentine & Gregg, 2008; Walker, 1973) and the transition from shallow fragmentation of rhyolitic magma to deeper cryptic fragmentation due to conduit blockage and sintering of the pyroclastic products, i.e., dome forming eruptions (Wadsworth et al., 2020).

Violent Strombolian eruptions are typically associated with the formation of scoria cones of various heights, widespread tephra blankets and extensive lava-flow fields (Pioli et al., 2008; Valentine et al., 2005). This eruptive style, as well as Vulcanian eruptions and long-lasting ash emissions, is difficult to classify solely based on tephra blankets and should be better characterized based on eruption dynamics and, particularly, on eruption unsteadiness (e.g., Coppola et al., 2022; Dominguez et al., 2016; Pioli et al., 2022). Eruption unsteadiness is mostly related to fluctuations of key physical parameters such as mass eruption rate (MER) on a wide range of time scales (seconds to hours or days) that result in the formation of several (tens to hundreds) thin layers (few to tens of millimeters) characterized by variable grainsize and/or clast texture and typology and/or color (e.g., Bonadonna et al., 2016; Pioli et al., 2008). Individual layers and units (sets of multiple layers having similar characteristics) in the stratigraphic record of long-lasting eruptions are of difficult spatial correlation, and associated cumulative isopach maps are typically subcircular, reflecting the wind variation over time, as it is often the case of violent Strombolian eruptions and Vulcanian cycles (e.g., El Jorullo 1759–1774, Mexico: Rowland et al., 2009; Parícutin 1943–1952, Mexico: Pioli et al., 2008; La Fossa, Vulcano 1888–1990, Italy: Di Traglia, 2011). The scale of unsteadiness (periodicity and amplitude of fluctuations) increases when passing from Plinian (quasi-steady), through sub-Plinian (oscillating, sustained, short-lived column), to violent Strombolian (lava fountain-fed, discontinuous, pulsating column-churn flow regime), to normal Strombolian (periodic rise of conduit-filling gas bubbles within the conduit-slug flow regime), to Vulcanian (discrete explosions separated by pauses; Bonadonna et al., 2016; Pioli et al., 2008). Long-lasting, hybrid eruptions are characterized by multiple shifts in style (e.g., normal Strombolian, violent Strombolian, Vulcanian, sub-Plinian) and are difficult to classify based on traditional strategies only considering tephra blankets (e.g., Volcanic Explosivity Index (VEI); Newhall & Self, 1982). First, tephra blankets are not the only product, with lava flows being often an important component (e.g., between 94 wt% of the magma erupted during the 1971 eruption of Etna and 39 wt% of the magma erupted during the Parícutin 1943–1952 eruption; Booth & Walker, 1973; Pioli et al., 2008; Walker, 1973). Second, tephra blankets are produced by long-lasting activity, and, therefore, the associated cumulative volumes cannot be compared with those of sustained, short-lived eruptions. Third, individual layers associated with individual eruptive pulses are of difficult spatial correlation and, therefore, associated volumes cannot be easily determined. Fourth, multiple vents, sometimes also associated with different eruptive styles, can be active at the same time producing complex tephra blankets. Fifth, the tephra blanket should be distinguished from tephra fallout that also includes the formation of the scoria cone, as we consider here. Finally, eruptive source parameters (ESPs) such as plume height, MER, total grainsize distribution, can fluctuate at various temporal scales (minutes to hours) during the eruption. Such a complexity and unsteadiness not only affect eruption classification but represent a major challenge also for ash dispersal forecasting based on Volcanic Ash Transport and Dispersal Models (VATDM), which typically assume sustained source term conditions over longer time scales (a few hours) (e.g., Beckett et al., 2020; Folch, 2012). Finally, the combination of effusive and explosive products emitted over a relatively long period of time makes hybrid eruptions particularly complex also in terms of crisis management and risk assessment because of the associated compound hazards and impacts (e.g., Carracedo et al., 2022; Fearnley & Beaven, 2018; Hicks & Few, 2015; Rees, 1979). In fact, ESPs need to be constrained for multiple processes (e.g., tephra plumes and lava flows; tephra plumes, lava domes, and pyroclastic density currents) at different time scales (hours to months); in addition, risk mitigation strategies require a broader understanding of the interaction between different physical processes such as the impact of lava flows and tephra deposits on the built environment and the impact of atmospheric convection induced by lava flows on the dynamics of tephra plumes and tephra dispersal (e.g., Deligne et al., 2017; Zuccaro et al., 2008). The evolution of the different styles over time is also of particular interest for an effective management of the volcanic crisis (e.g., Sword-Daniels et al., 2013). As a

result, a better understanding of the dynamics of hybrid eruptions is necessary both to eruption characterization and to reduce the associated risk.

The September–December 2021 eruption of Cumbre Vieja (La Palma Island, Spain), recently named *Tajogaite eruption*, represents a typical example of long-lasting, hybrid eruption with alternation, or, more often, contemporaneous emission, of lava flows and tephra (Longpré, 2021; Pankhurst et al., 2022; Romero et al., 2022a). An additional complication of this eruption was the presence of multiple vents mostly active at the same time associated with different styles of explosive activity (e.g., ash emissions, lava fountains, Strombolian activity) as well as multiple active vents producing lava flows over a fissure of about 0.5 km. The eruption classification as well as the forecasting of associated ash dispersal were challenging, with rapidly varying ESPs and wind conditions.

With the objective to illustrate the temporal scale of eruptive unsteadiness and fluctuation of the 2021 Tajogaite eruption, this work characterizes the associated tephra blanket in combination with the analysis of lava emission rate, tephra cone, atmospheric wind, and volcanic tremor. In particular, a detailed analysis of the stratigraphy is presented together with the description of individual eruptive phases and the characterization of key ESPs over time and all associated uncertainties (i.e., duration, plume height, erupted volume and mass, MER). Implications for eruption classification and ash dispersal forecasting are also discussed. To be noted that data on grain size are not included here for a matter of space and will be presented in a future paper.

## 2. Background

### 2.1. Geological Setting

La Palma Island is part of the Canary archipelago, one of the most active volcanic regions of the planet (Abdel-Monem et al., 1972; Carracedo et al., 1998). Subaerial volcanic activity in the archipelago began around 20 Ma ago building the eastern Canary Islands, Lanzarote, and Fuerteventura. Among the seven largest islands, La Palma is historically the most active of the Canary Islands with relatively frequent eruptions from the Cumbre Vieja rift zone that includes the 1585, 1646, 1677–1678, 1712, 1949, and 1971 eruptions, before the 2021 Tajogaite event (Carracedo et al., 1998, 2001; Casillas et al., 2020; Klügel et al., 1999). Volcanic history at La Palma dates to 3–4 Ma, when a submarine basal complex of seamounts started to form (Carracedo et al., 1999; Staudigel et al., 1986). Following subaerial activity (850–560 ka; Carracedo et al., 2001) contributed to the formation of Garafia and Taburiente shield volcanoes, the Cumbre Nueva rift zone, and the Bejenado volcano complex. This oldest subaerial volcanism is well recognizable in the northern sector of the island and suffered from repeated, large lateral collapses (Ancochea et al., 1994; Carracedo et al., 2001; Day et al., 1999). A progressive decline in volcanic activity at Bejenado and Taburiente volcanoes pushed volcanism southwards where the Cumbre Vieja rift zone formed at about 125 ka. Since then, this area hosts the presently active volcanic system on La Palma, characterized by multivent activity generally aligned along kilometer-long fissures erupting silica undersaturated basanite and alkali basalts (Barker et al., 2015; Carracedo et al., 2001; Day et al., 1999).

### 2.2. Chronology and Atmospheric Conditions of the 2021 Tajogaite Eruption

On 19 September 2021, a new magmatic eruption started in the Cabeza de Vaca area, on the western flank of the Cumbre Vieja ridge, that lasted about 86 days; it was preceded by a few years of relatively deep (25–35 km) and low-magnitude seismic activity, and by 1 week of intense seismic unrest and ground deformation (Carracedo et al., 2022; Civico et al., 2002a; Fernández et al., 2021; Romero et al., 2022a; Torres-González et al., 2020; Wadsworth et al., 2022). The initial eruption vent gradually developed into an NW–SE fissure, about 0.5-km long, resulting from the emplacement of a westerly dipping feeding dyke, which represents an NW continuation of the normal faulting system associated with the 1949 eruption (Carracedo et al., 2022; González, 2022; Pankhurst et al., 2022). The final eruptive structure consists of a new scoria cone (recently named *Volcán de Tajogaite*) of about 1,130 m above sea level (a.s.l.) (i.e., 187 m above the previous level; Civico et al., 2022a) associated with six vents, with five additional vents that developed further North (Plan de Emergencias Volcánicas de Canarias—PEVOLCA—reports: <https://www.gobiernodecanarias.org/infovolcanlapalma/pevolca/>; Carracedo et al., 2022; Romero et al., 2022a). The SE vents were mostly associated with the generation of tephra plumes and lava fountains (Figure 1), while the NW vents were mostly associated with the generation of lava flows and passive degassing (Romero et al., 2022a). An Unoccupied Aircraft System (UAS) survey provided a volume of the final scoria cone of  $36.5 \pm 0.3 \times 10^6 \text{ m}^3$  ( $8.9 \pm 0.2 \times 10^6 \text{ m}^3$  on 27 September 2022; Civico et al., 2022a, 2022b). The

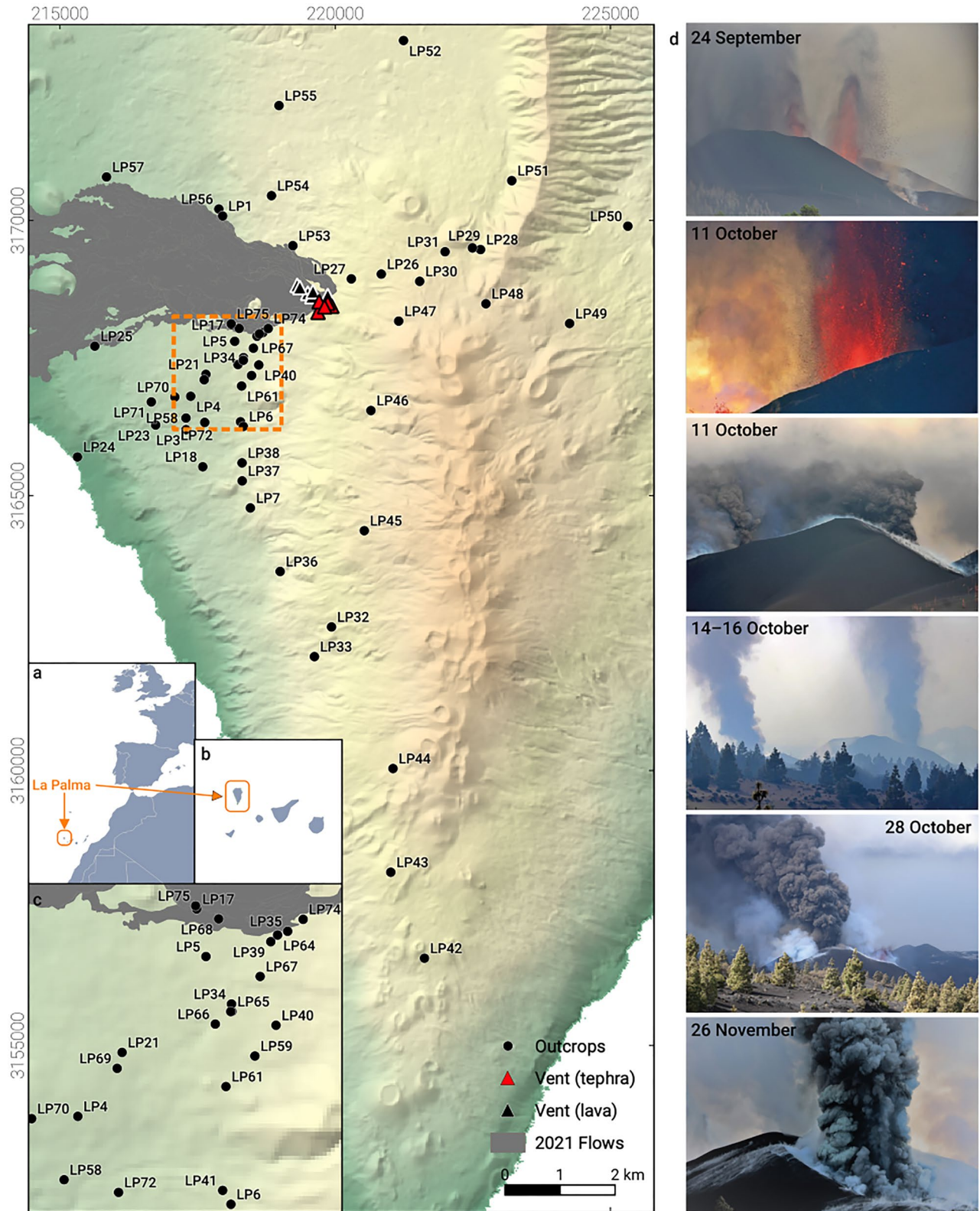
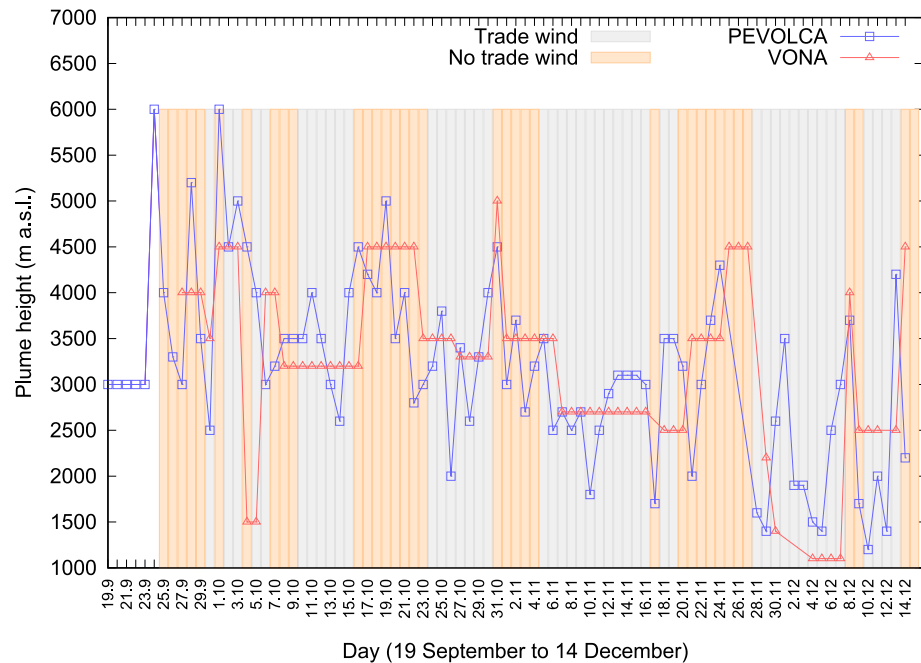


Figure 1.



**Figure 2.** Height of tephra plumes (in m a.s.l.) as reported in the PEVOLCA reports (blue squares) (<https://www.gobiernodecanarias.org/infovolcanlapalma/pevolca/>) and in the Volcano Observatory Notice for Aviation (VONA; red triangles) compiled by the Instituto Geográfico Nacional (IGN; e.g., Felpeto et al., 2022) and used by the Volcanic Ash Advisory Center (VAAC) of Toulouse to make daily forecasts (<http://vaac.meteo.fr/volcanoes/la-palma/>). Plume height observations were mostly made in the morning for the PEVOLCA reports and during different times of the day for the VONA using the camera of the Instituto Astrofísico de Canarias (IAC) located at 2,365 m a.s.l. and 16.5 km north of the main vents. Average of both PEVOLCA and VONA reports results in a value of 3.2 km a.s.l. even though observations were taken at different times during the day and data set of VONA only starts after 27 September. The highest plumes observed during the eruption on 12–13 December (6.0 and 8.5 km a.s.l.) are not shown as they occurred in the afternoon and were not reported in the VONA. Gray vertical bars indicate days dominated by Type 1 wind (sustained trade winds), while orange vertical bars indicate days mostly characterized by Type 2 winds (inexistent or weak trade winds) (see text for details and implications). Wind observations are available only after 25 September 2021.

combined effusive and explosive activity built a  $\sim 12$  km<sup>2</sup> lava-flow field on the west side of the island and a widespread tephra blanket associated with pulsating plumes with average height of about 3.2 km a.s.l. (Figure 2), even though plumes up to 6.0 and 8.5 km were observed on December 12 and 13, respectively (PEVOLCA reports). Lava flows reached the ocean on September 28 forming a new lava delta and interacting with sea water producing lava haze (i.e., laze). In addition, the eruption produced large amounts of SO<sub>2</sub> that were detected as far as the Caribbean and Central Europe and was accompanied by diffuse emission of CO<sub>2</sub> associated with the 220 km<sup>2</sup> of the Cumbre Vieja volcanic ridge (PEVOLCA reports). Thanks to the implemented scientific monitoring and management policies, direct human fatalities from volcanic activity were avoided. Nonetheless, the Tajogaite eruption significantly impacted the SW of the island, caused the evacuation of almost 8,000 people, and affected more than 2,800 buildings as well as about 1,000 ha of plantations and farmland; in addition, the lava-flow field cut the western part of the island in two, generating significant disruption to the transport system and to the accessibility to key municipalities (Carracedo et al., 2022). Volcanic gas (CO<sub>2</sub> and SO<sub>2</sub>) and ambient concentrations of fine particulate volcanic matter (PM10) also caused severe disruption, forcing repeated confinement of communities and the cessation of public activities (e.g., schools) beyond the area of direct impact (Carracedo et al., 2022).

**Figure 1.** Map of sample locations studied in this paper (see Table S1 in Supporting Information S1 for detailed description). Inset (a) shows the location of the Canary Islands; inset (b) shows the location of La Palma; inset (c) zooms on the orange box on the main map. (d) Different eruptive styles that characterized the eruption are shown with examples of tephra plumes (11 October, 14–16 October, 28 October 2021), lava fountains (24 September, 11 October 2021), and steam-loaded tephra plumes (26 November 2021) associated with various eruptive phases (Credit photo of 24 September 2021: Miguel Calero). Lava field in (a) traced with data from Copernicus Emergency Management Service (© 2021 European Union), EMSR546.

The general atmospheric circulation in La Palma is characterized by prevailing low-level NE trade winds (i.e., blowing toward SW) driven by the subtropical high-pressure belt (the Azores anticyclonic system) and that alternate cycles of increased intensity and calm (Carrillo et al., 2016). Depending on the elevation of the thermal inversion cap, trade winds lifted upwards by the island's orography (Cumbre Nueva and Cumbre Vieja ridges) can either result on downslope winds (foehn winds, when the inversion cap lays above  $\sim 1,500$  m a.s.l.) or be diverted and generate complex low-level leeside recirculation (no foehn winds, inversion cap below  $\sim 1,500$  m a.s.l.). The thermal inversion also affects relative humidity, with values of 70%–80% (wet unstable conditions) and 10%–30% (dry stable conditions) below and above the inversion layer, respectively. During no inversion and calm situations (weak synoptic winds), local wind patterns can also be affected by land/sea breezes and convective motions, an aspect that was exacerbated by the presence of an extended hot lava field. On the other hand, trade winds can veer higher in the troposphere (above the thermal inversion) to blow toward NE (anti-trade winds). Days of the eruption period were grouped in two categories: Type 1 (days in which trade winds were stronger, resulting in a relatively stable dispersal between S and W, SW being the predominant direction), and Type 2 (days in which trade winds were weaker or inexistent, resulting in oscillating dispersal direction, in some cases with a rotation of almost  $360^\circ$  during the same day; Figure 2). Orography and trade winds also control precipitations in the island, producing a typical precipitation gradient from a humid NE windward side ( $\sim 1,400$  mm maximum) to a dry leeward coast in the SW of the island ( $\sim 170$  mm maximum; Irl et al., 2015). November and December represent the wettest months in La Palma. In particular, on 26 November, nearly 20 mm of rain fell on the island producing steam-loaded tephra plumes (PEVOLCA reports; Figure 1d).

### 3. Methods

Field work was carried out both during the eruption (October–November 2021) and after the end of the eruption (February 2022 and May 2022). The first campaign mostly focused on the stratigraphic analysis of the tephra blanket based on excavated trenches and collection of tephra samples for deposit density at selected sections. During the second and third campaigns, selected sections analyzed during the eruption were revisited to update the stratigraphy and to collect new samples; additional complete sections were also investigated to compile isopach maps of the total deposit, individual units, and selected layers (Figure 1).

#### 3.1. Stratigraphy

We investigated 45 outcrops from proximal ( $\sim 0.7$  km) to distal ( $\sim 12$  km) areas to define the stratigraphic architecture of the tephra blanket and to cross-check deposit characteristics with the available chronology and direct observations of the eruptive events (Figure 1 and Table S1 in Supporting Information S1). At each site, a detailed stratigraphic log of tephra horizons was measured and described, and the whole sequence was correlated among the different outcrops. Based mainly on sedimentologic (grainsize and size grading of deposits) and changes of lithological (color, density/vesicularity of clasts) features, the tephra sequence was organized into layers and sublayers, representing multiple eruptive phases, and single eruptive pulses, respectively. Layers were further grouped into units, representing longer eruptive periods. Particularly, the qualitative variability of the abundance of the juvenile and lithic components as well as the characteristics of the juveniles (color, shape, vesicularity) were used in the field to discriminate among the different layers and afterward confirmed in the lab under binocular microscopy observations. Several key sections, from proximal to distal areas, were particularly useful to trace correlations between different sublayers, layers, and units and to reconstruct a total stratigraphic sequence that comprises all the products emplaced during the whole eruption. In particular, the individual units, layers, and sublayers were analyzed in detailed at one of our most proximal locations SW of the vents (LP35 in Figure 1) with qualitative description of the different components. A quantitative description of the size of the largest scoria clasts is presented for the two most proximal locations SW (LP35) and NE (LP27) of the vents.

#### 3.2. Determination of the Largest Scoria Clasts

The 20 largest clasts were collected out of 100 clasts with a diameter  $>1$  cm for the coarsest layers at the two most proximal locations NE and SW of the vents (LP27 and LP35, respectively; Figure 1); the 50th percentile was determined based on the geometric mean of the three associated axes (measured based on the technique of Bagheri and Bonadonna (2016)). The 50th percentile of the 20 largest clasts is representative of the largest clasts

of a given outcrop, which provide insights into plume height (Bonadonna et al., 2013). Such a measurement was considered as a proxy for the variation of plume height in time (within the same outcrop) and for the variation of grainsize NE and SW from the vent.

### 3.3. Determination of Volume, Mass, and MER of the Tephra Blanket

The volume of the total tephra blanket, individual units, and selected layers was determined based on the integration of the exponential, power law, and Weibull empirical fitting of deposit thickness versus square root of area of isopach contours (Bonadonna & Costa, 2013; Bonadonna & Houghton, 2005; Pyle, 1989) using the TephraFits tool of Biass et al. (2019). The uncertainty on volume was quantified using the bootstrapping method of Biass et al. (2014), repeating 10,000 volume calculations by varying input parameters to account for various sources of uncertainty (i.e., area of isopach contours, distal integration limits of the power law; Bonadonna et al., 2015; Klawon et al., 2014; Table S2 in Supporting Information S1). Volume was converted to mass using the bulk density of the tephra blanket. MER was determined combining erupted mass and eruption duration. We account for the uncertainty on density and eruption duration by stochastically sampling 10,000 values of each from a Normal distribution, resulting in distributions of values of volume, mass, and MER that propagate uncertainties (Table S3 in Supporting Information S1). Each parameter is reported as the median and the 90% confidence interval. Propagation of uncertainty associated with the volume, mass and MER of the tephra blanket, cone and lava is also determined (Table S4 in Supporting Information S1).

### 3.4. Determination of Lava Emission Rates and Volume

The lava emission was estimated using satellite thermal data processed by the MIROVA system which is based on the analysis of MODIS (Moderate Resolution Imaging Spectroradiometer) infrared data with a resolution of 1 km<sup>2</sup> (Coppola et al., 2020). The system is operational in near real-time (acquiring ~4 images per day over La Palma) and processes the MODIS images to detect the presence of high-temperature thermal anomalies, and to calculate the associate Volcanic Radiative Power (VRP in Watts). The effusive trend and the volumes of the lava flow were calculated using the method described by Coppola et al. (2013, 2019), which assumes a direct relationship between VRP and the Time Averaged lava Discharge Rate (TADR)

$$\text{TADR} = \frac{\text{VRP}}{c_{rad}}$$

where  $c_{rad}$  embeds the rheological, insulation, and topographic conditions appropriate for the observed lava flow into a unique best-fit parameter (Coppola et al., 2013). Here, we set  $c_{rad}$  equal to  $2 \times 10^8 \text{ J m}^{-3}$ , a value which is typical for basaltic lava flows (Coppola et al., 2013, 2019). This method permits the estimation of the TADR with an uncertainty of  $\pm 50\%$ , which takes into account the systematic errors in the calculation of VRP as well as the variable conditions for the emplacement of the lava flow (Coppola et al., 2019). In particular, the uncertainty on the degree of thermal insulation is  $\pm 30\%$  (i.e., standard error associated with the impossibility of knowing both the area and the integrated temperature of the lava flow based on one single band—the midinfrared used by MIROVA). In order to convert the heat flux (VRP) to volumetric flux (TADR), other factors related to the emplacement conditions of the lava flow are required such as the rheology of the lava (rheological conditions) and the topography of the substrate. Based on the empirical analysis of several eruptions around the world, the overall error associated with all these factors (thermal insulation and both rheological and topographic conditions) has been estimated to  $\pm 50\%$  (Coppola et al., 2013). It is important to note that the thermal approach provides bulk estimates of the subaerial lava volumes, capable of radiating thermal energy into the atmosphere. The final estimated volume ( $170.3 \pm 85.1 \times 10^6 \text{ m}^3$ ) is, therefore, a minimum estimate as it ignores the submarine part of the lava flow below the lava deltas. Such an estimate agrees with the estimate of subaerial lava flow ( $177.6 \pm 5.8 \times 10^6 \text{ m}^3$ , including tephra blanket on lava flows) provided by UAS-based photogrammetry (Civico et al., 2002b, 2022a).

### 3.5. Density of Tephra Blanket, Scoria Cone, and Lava Flow

The deposit density of most individual layers and of individual units was determined in the laboratory based on the weight of individual samples dried in the oven at 80° and associated volume as measured in graduated cylinders. Values were averaged over five measurements with variations estimated within 10%. Values measured in the lab showed good agreement with values of density for selected outcrops based on the weight of the deposit dried in the oven and the volume as determined in the field. The density of the proximal deposit (<1.5 km from vents) was considered to estimate the density of the cone, in agreement with observations for basaltic cones at Etna volcano (Italy; e.g., McGetchin et al., 1974; Pioli et al., 2022). Lava density was determined based on the model DensityX (Iacovino & Till, 2019) and the data set of Castro and Feisel (2022) (i.e., composition, water, temperature, and pressure), resulting in a value of  $2,770 \pm 50 \text{ kg m}^{-3}$ . This value well agrees with the density of the lava that was measured on 10 samples collected between 26 September and 6 October 2021 using a Helium Pycnometer resulting in a value of  $2,618 \pm 179 \text{ kg m}^{-3}$ .

### 3.6. Seismic Tremor Data

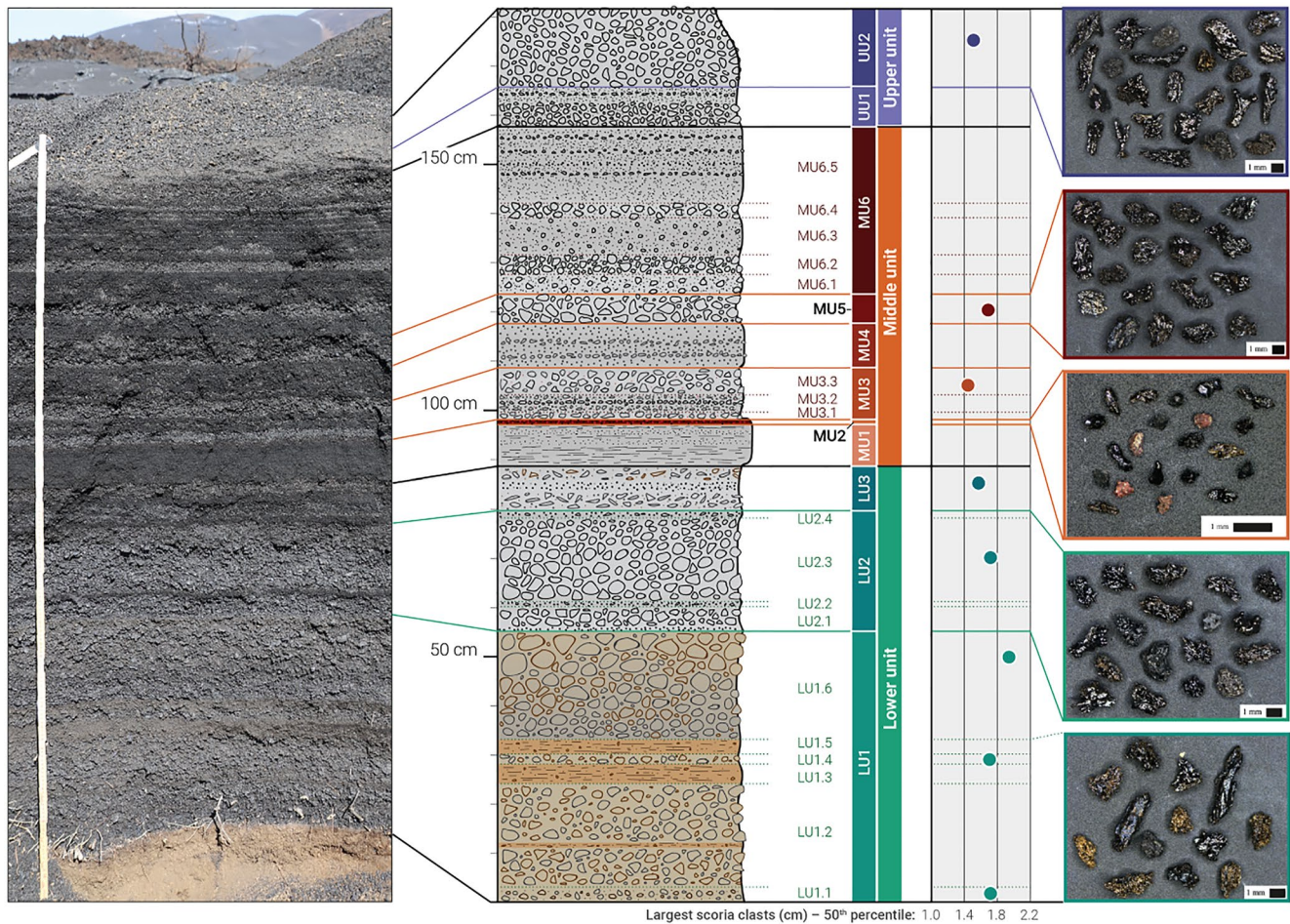
The volcanic tremor amplitude has been computed by averaging the envelope of the vertical component of the seismic station PTAB, operated by INVOLCAN (Instituto Volcanológico de Canarias), located about 7.5 km NNW of the vents, over 1-min-long time windows. The volcanic tremor amplitude has been computed over two frequency bands: the Very-Long Period (VLP; 0.4–0.6 Hz) and the Long Period (LP; 1–5 Hz), being these two frequency ranges where the average spectral amplitudes of the tremor were higher. Taking into account the local *S* wave velocity model (D'Auria et al., 2022), we state that the wavelengths associated with Rayleigh waves in the VLP component are between 2.5 and 3.5 km, while for the LP component are between 0.3 and 1.5 km. This means that the VLP component reflects the dynamics of the first few hundred meters, while the LP components of the first tens of meters depth within the conduit. Therefore, the ratio between the LP and the VLP amplitudes should detect changes in the eruptive dynamics, such as conduit widening and/or variations in the explosive mechanism.

## 4. Results

### 4.1. Stratigraphy

Three tephra units and 11 layers have been identified based on the analysis of the final tephra blanket and correlated among all the surveyed stratigraphic sections (Figures 3 and 4). This stratigraphy is consistent with a detailed study carried out for the first part of the eruption (Romero et al., 2022a) and in agreement with the reconstruction proposed by collective work carried out under the umbrella of INVOLCAN. The Lower Unit (LU) is lapilli-size dominated with intercalation of fine-to-coarse ash layers and includes three main layers (LU1–3); the Middle Unit (MU) is fine-to-coarse-ash dominated, with intercalation of lapilli layers, and includes six main layers (MU1–6); the Upper Unit (UU) is dominated by lapilli-sized clasts and consists of two main layers (UU1–2) (Figure 3). Up to six sublayers have also been identified within some of the thickest layers (LU1.1–6, LU2.1–4, MU3.1–3, MU6.1–5). Within a radius of 5 km from the vents, the tephra sequence is dominated by multiple lapilli-bearing fallout layers alternated with centimeter-thick to millimeter-thick, ash-rich fallout sublayers, with all layers and sublayers clearly recognizable. The whole tephra sequence tends to thin out very rapidly (Figure 4). As a result, while in proximal areas (<5 km from vents) most of the layers and sublayers can be identified and correlated, in medial and distal areas (>5 km from vents) only the separation of the different main units is possible. In fact, the marked sedimentological differences (namely color, grain size, and componentry), allowed a first-order separation across the three main units which can be confidently traced up to the distal limits of the fallout deposit on land (12 km). Note that the term proximal (<5 km from vents), medial (5–10 km from vents), and distal (>10 km) are based on the analysis of the tephra blanket on land that could be carried out only down to 12 km from the vents. Overall, the whole tephra sequence is characterized by a strikingly fresh appearance with negligible proportions of altered lithic clasts. The fresh, juvenile clasts can further be subdivided based on their color, vesicularity and morphology, with relative proportions varying between individual units, layers, and sublayers, particularly at proximal locations. Thickness of the total tephra blanket, of all units and of selected layers at the studied locations are reported in Table S1 in Supporting Information S1.

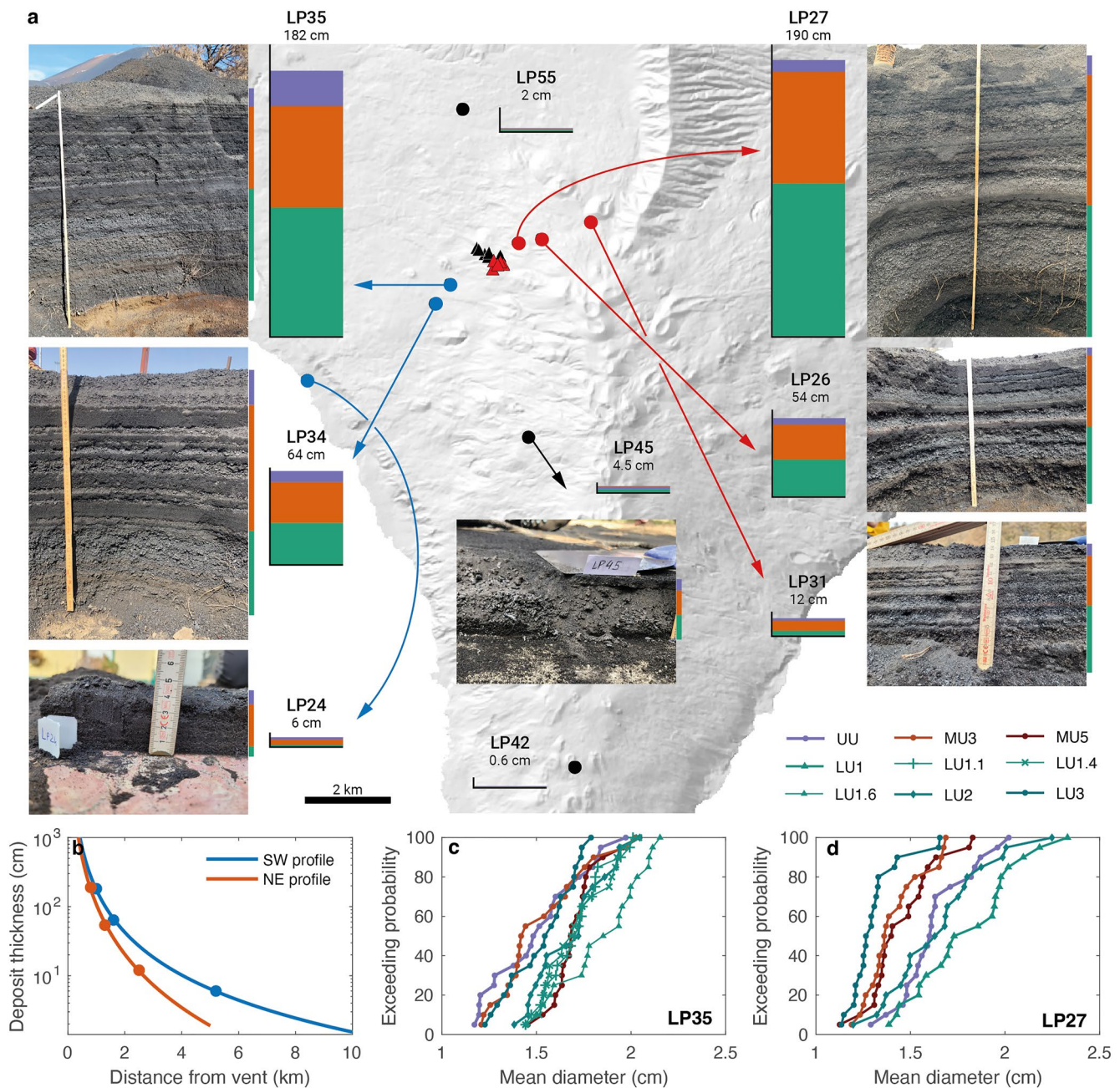




**Figure 3.** Reference stratigraphic section ~1 km SW of vents (LP35 in inset a) of Figure 1 showing: 3 different units (Lower, Middle, Upper), 11 layers (LU1, LU2, LU3, MU1, MU2, MU3, MU4, MU5, MU6, UU1, UU2), and 18 sublayers (LU1.1–6, LU2.1–4, MU3.1–3, MU6.1–5); the 50th percentile (in cm) of the population of the 20 largest scoria clasts for selected layers and sublayers (LU1.1, LU1.4, LU1.6, LU2.3, LU3, MU3.3, MU5, UU2); and representative clasts for selected layers and sublayers in various size ranges (LU1.1–1.5: 1–1.4 mm, LU2: 1–1.4 mm; MU2: 250–355  $\mu$ m; MU5: 1–2 mm; UU2: 1–2 mm).

#### 4.1.1. Lower Unit (LU)

The LU is a lapilli-size dominated unit intercalated with fine-to-coarse ash. It is made of three layers (LU1, LU2, and LU3) and comprises the coarsest deposits of the eruption. LU has an overall thickness ranging from about 1 to 100 cm (Figures 3 and 4; Table S1 in Supporting Information S1). Specifically, LU1 is further divided in six sublayers (from LU1.1 to LU1.6) mainly composed of massive, moderately to poorly sorted, brownish lapilli layers alternated with massive, moderately sorted, brown ash layers with scattered lapilli (Figure 3). The characteristic brown color of LU1 is due to the presence of light-colored, frothy, vesicular glass (Figure 3). This component shows a homogeneous vesicularity with small vesicles and irregular clast morphologies. The other dominant component involves fresh dark glass characterized by smooth surfaces, with fluidal, elongated morphologies, and variable vesicularity. While in the stratigraphically lower sublayers (e.g., LU1.1), the dark juvenile glass shows a fresh, glassy appearance, with increasing stratigraphic height, the surfaces of dark fluidal glass appear increasingly dull and opaque. Due to its brownish color, layer LU1 can be easily identified in proximal to medial outcrops, and its thickness varies from 55 cm (1 km from the cone) to 0.2 cm (5 km W of the vent; Table S1 in Supporting Information S1). At distances >5 km, LU1 becomes difficult to identify. A change in color of the emplaced material marks the transition from LU1 to LU2, with the latter being further subdivided in four sublayers (from LU2.1 to LU2.4). These sublayers are made of massive to normally graded, poorly sorted, gray lapilli-bearing layers alternated with gray-to-black ash layers. In line with the evident color change in the deposit, LU2 contains mostly dark juvenile glass, while the light-colored frothy juvenile glass becomes



**Figure 4.** Variation of (a) stratigraphy (consistently with colors in Figure 3, violet, orange, and green colors indicate the Upper Unit (UU), Middle Unit (MU), and Lower Unit (LU), respectively) and (b) deposit thickness with distance from the vents for selected locations fitted by a power law (LP35, LP34, and LP24 SW of the vents and LP27, LP26, and LP31 NE of the vents). Location N (LP55) and S (LP45 and LP42) of the vents are also shown for comparison. Population of the 20 largest scoria clasts at locations (c) LP35 (SW of the vents) and (d) LP27 (NE of the vents) are shown (see Figure 3 for 50th percentile of the populations of LP35).

subordinate (Figure 3). Here, the dark glass has a characteristically iridescent appearance with smooth, glassy surfaces and fragile, angular, fluidal, and elongated morphologies. Other dark-colored juvenile components show irregular morphologies with variable vesicularity, ranging from less translucent glass with larger vesicles and thicker bubble walls to brown translucent glass with small vesicles and thin bubble walls. The upper sublayer LU2.4 displays an overall decrease in vesicularity as witnessed by the presence of scoriaceous glass with dense groundmass and isolated large vesicles, as well as sparse dense components with irregular morphologies. Scattered scoriaceous clasts display a dull, gray surface, while others show a red color and evidence of oxidation. The thickness of LU2 varies from 0.3 to 37 cm (Table S1 in Supporting Information S1). LU3 represents the upper

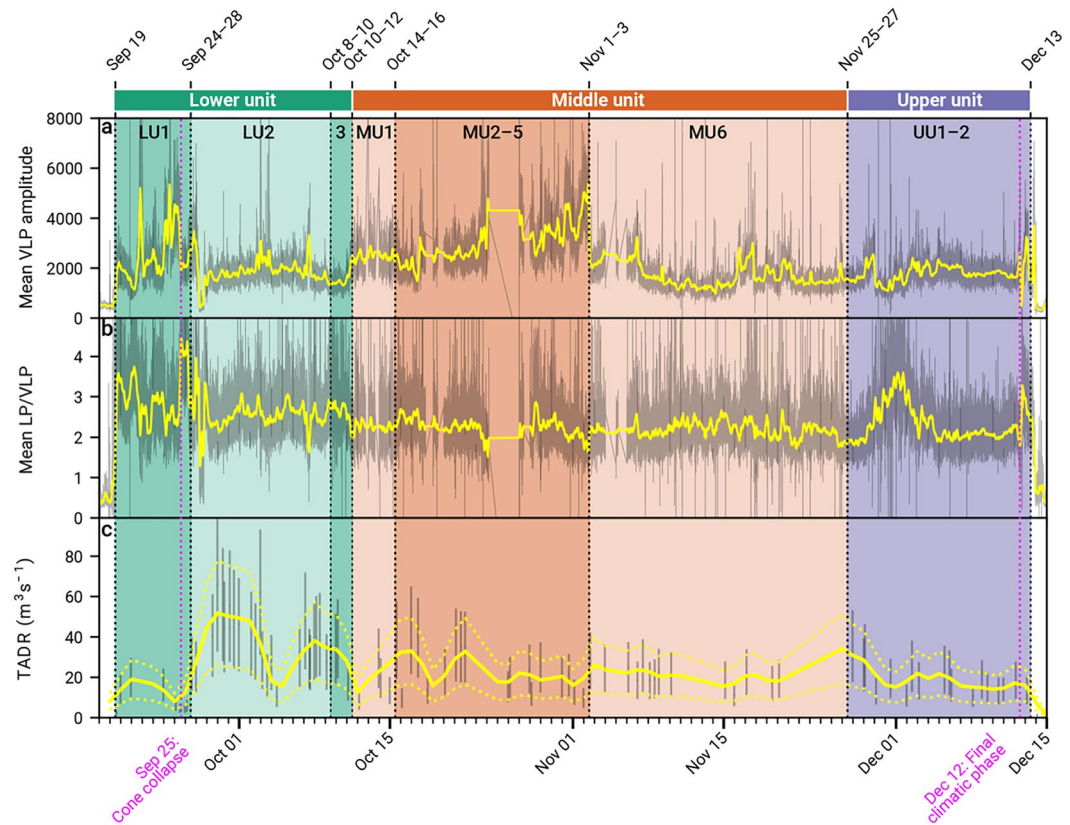
part of LU and is represented by a massive, coarse ash to lapilli-bearing layer, varying in thickness from 0.2 to 4.5 cm. This unit is composed mostly of dark-colored, iridescent, fluidal vesicular glass with smooth surfaces, together with characteristic vesicular golden glass that exhibits elongated and stretched, fluidal morphologies, yielding an overall high clast vesicularity for this unit. However, compared with the underlying sublayers, an increase in the proportions of components with dense groundmass can be observed. These components comprise fresh scoriae with heterogeneous vesicle distribution including large vesicles, and an irregular morphology as well as dull scoriae with dense groundmass, variable vesicularity, and thick bubble walls. Sporadic red oxidized scoriae with dense groundmass and variable vesicle distributions can be identified as lithics.

#### 4.1.2. Middle Unit (MU)

The MU is a fine-to-coarse-ash-dominated unit intercalated with lapilli layers; associated thickness ranges between about 1 and 76 cm (Figures 3 and 4; Table S1 in Supporting Information S1). An abrupt change in grain size marks the transition from LU to MU, with ash-dominated beds becoming increasingly abundant from base to top and when compared with LU, where lapilli-bearing beds were dominant. We identified a massive, coarse, black ash-bearing layer (MU1) at the base of the MU. Compared to LU, juvenile components in MU1 are characterized by a marked decrease in vesicularity. Juvenile clasts comprise mostly scoriaceous glass with heterogeneous vesicle distributions, thick bubble walls and irregular morphologies as well as blocky particles with a dense groundmass (Figure 3). The surfaces are characterized by a dull appearance. Few scattered clasts with smooth surfaces and fluidal, stretched morphologies are observed. In line with the overall finer grain size of this unit, pyroclast surfaces often display a fine ash cover. MU2 represents a widespread distinctive ~mm-thick, red, oxidized fine-to-coarse ash-bearing layer that is clearly visible within the sequence and was used as a guide horizon. The remarkable reddish color is due to the presence of oxidized dense blocky lithics and scoriae, which can be found mostly in the fine ash fraction (Figure 3). Contrastingly, the coarser fractions comprise fresh-looking juvenile glass of dark color, with smooth surfaces and elongated fluidal morphologies as well as brown translucent glass with irregular, elongated, angular morphologies. Furthermore, juvenile dense and scoriaceous components with a dull surface and dense groundmass are observed. While MU2 is the most distinctive red-lithic rich layer that was used as a marker to help correlate the whole stratigraphy at different distance from the vent, scattered red lithic clasts are present throughout the layers MU2–MU6. Layer MU3 overlies the red ash layer of MU2; it comprises a series of three beds (MU3.1, MU3.2, MU3.3) that consist of massive, poorly sorted, gray, coarse ash to lapilli. On top of MU3, layer MU4 is made of an alternation of black, coarse ash with gray lapilli-bearing layers ranging in thickness from 0.5 to 11 cm. Overall, the componentry of MU3 and MU4 is characterized by the presence of dark fresh, fluidal glass with stretched and elongated morphologies and brown glassy clasts with small homogeneous vesicles. Fresh, irregular scoriaceous clasts with large vesicles and thick bubble walls as well as scattered dense clasts with blocky morphologies represent the less vesicular component. MU5 is the coarsest layer of MU, being a massive, poorly sorted, brown to black lapilli-bearing layer with a thickness ranging from 0.5 to 16 cm (Table S1 in Supporting Information S1). It has a very fresh appearance, containing predominantly black clasts of variable vesicularity with smooth, metallic surfaces and fluidal, elongated morphologies as well as vesicular, translucent glass with irregular morphologies and heterogeneous vesicularity; clasts with a dull surface, including both those with dense groundmass as well as variably vesiculated scoriae, are subordinate (Figure 3). MU6 represents the top of MU, being further divided in five sublayers (MU6.1–MU6.5) and is characterized by an alternation of massive, moderately to poorly sorted, gray-to-black coarse ash. Compared to the underlying unit, MU6 displays higher proportions of dull scoriae, including both dense clasts with blocky morphology and clasts of variable vesicularity and with irregular morphology. Some show evidence of superficial, red oxidation. The fresh-looking, juvenile component displays smooth, metallic surfaces, similar to the underlying sublayers and shows variable vesicularity, ranging from clasts that are dense, glassy, and with fluidal, rounded morphologies to more vesicular glass that appears very fragile with angular, fluidal morphologies to microvesicular, translucent glass. Relative proportions of the different components vary within MU6: from bottom to top layers, an overall increase in vesicularity can be observed, while the proportions of fluidal clasts with smooth surface decreases.

#### 4.1.3. Upper Unit (UU)

The UU seals the whole tephra sequence and shows a thickness range between 0.2 and 24 cm (Figures 3 and 4; Table S1 in Supporting Information S1). The uppermost part is sporadically and partially reworked by wind and water. Two layers can be well identified in the proximal locations SW of the vents (UU1 and UU2, respectively; Figure 3). UU1 is a normally graded, poorly sorted, gray ash to lapilli layer with scattered lithics, ranging in



**Figure 5.** Four-hour moving average (yellow line) of tremor data from the PTAB station of INVOLCAN during the eruption showing (a) the mean Very-Long Period (VLP) amplitude and (b) the average of mean Long Period (LP)/VLP. Gray values show the raw, unfiltered data. (c) Two-days moving average of Time Averaged lava Discharge Rate (TADR; yellow line). Gray values show the raw data with a symmetrical  $\pm 50\%$  measurement error. Yellow dotted lines show a symmetrical  $\pm 50\%$  envelope around the average value. Black vertical lines (plotted at midday) indicate the best guess of transition between different layers and units (interval is shown on the secondary horizontal axis; see also main text and Figure S1 in Supporting Information S1 for more details on these transitions). Pink vertical lines indicate two important events: cone collapse of 25 September and beginning of the final climatic phase started on 12 December with plumes up to 6.0 and 8.5 km a.s.l. (PEVOLCA reports; Romero et al., 2022a).

thickness from 0.2 to 10 cm. UU2 represents the top of the sequence and is a massive, moderately sorted, gray lapilli-bearing layer with a maximum thickness of 7 cm, although the separation among UU1 and UU2 is often difficult to constrain. UU1 is characterized by an overall dark color with fluidal glass with smooth surface being particularly elongated. Other juvenile glass is characterized by higher vesicularity while being more equidimensional with irregular morphologies. Components with a dull surface are subordinate and consist in dense blocky clasts and variably vesiculated scoriae. In UU2 the fluidal, elongated glass is characterized by less smooth surfaces and more irregular, angular morphologies (Figure 3). Relative proportions of dull clasts with irregular and blocky morphologies, as well as dull scoriae with heterogeneous vesicle distributions and irregular morphologies decrease compared to the underlying bed. On top of UU2, particularly in the area proximal to the cone, decimetric to metric bombs were emplaced to form a bomb field, representing the latest stage of the eruption.

#### 4.2. Duration of the Eruptive Phases From Direct Observations and Seismic Record

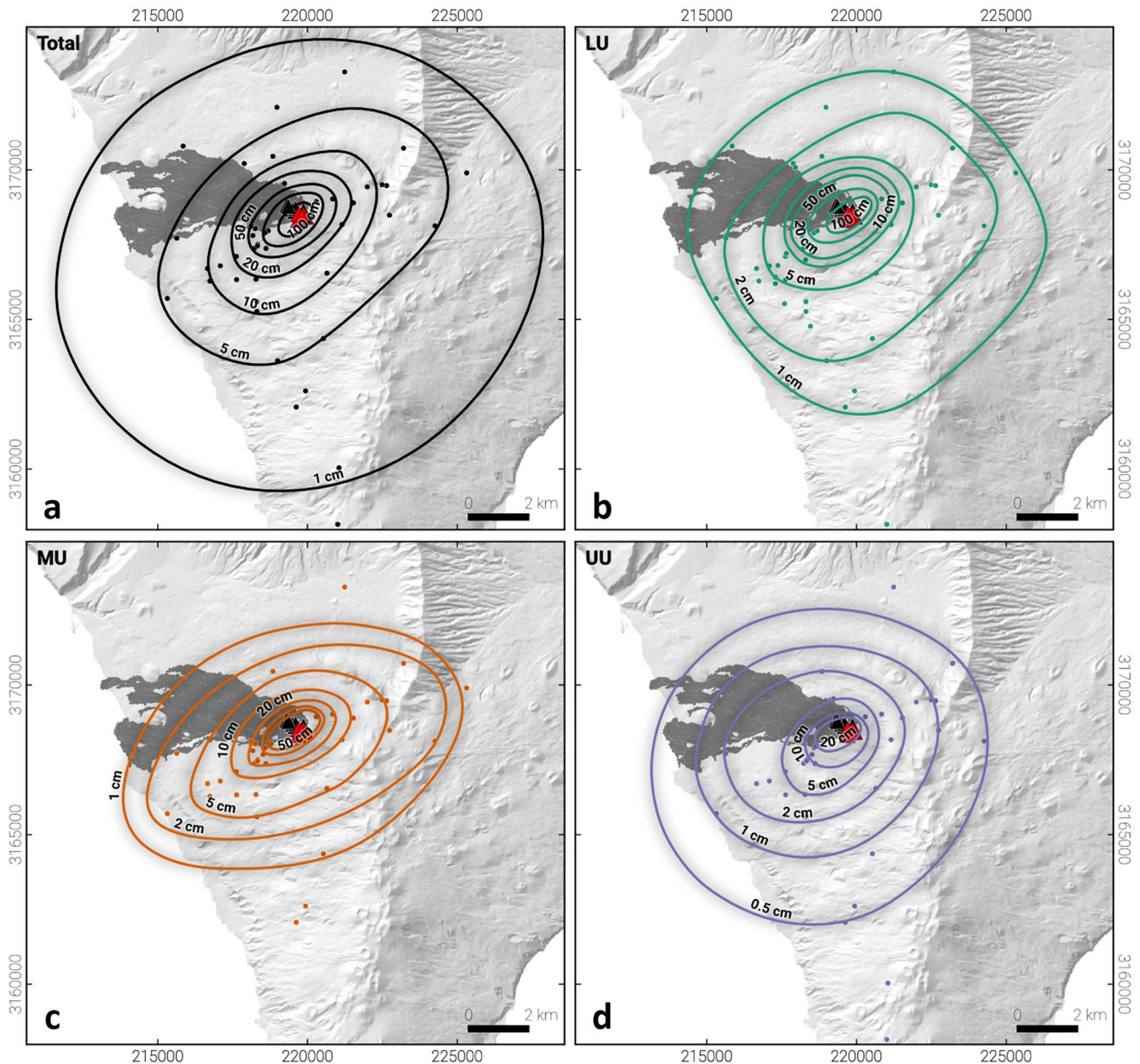
Duration associated with all individual units and selected layers (Figure S1 in Supporting Information S1) was determined based on direct observations (Figures S2–S9 in Supporting Information S1) and compared with tephra collection based on the tray network operated by the INVOLCAN team. Transition amongst units and key layers well correlate with both the volcanic tremor as recorded by the PTAB station and the TADR (Figure 5). Given the difficulty of identifying a clear temporal transition between individual units and layers, an uncertainty of  $\pm 1$  day for LU and UU (for which onset and end is well constrained) and of  $\pm 2$  days for the remaining layers and units

is considered (Figure S1 in Supporting Information S1). The temporal transition of most layers of the MU and of the two layers of the UU could not be easily constrained even within this level of uncertainty. In general, volcanic tremor associated to Strombolian activity shows a good correlation with explosive activity (Chouet et al., 1997; Ripepe et al., 1996). As explained in Section 3, we consider volcanic tremor amplitude both in the VLP and in the LP band. The VLP signal has been explained with the sudden expansion of gas pockets rising in the liquid melt in the deeper portion of the conduit (D'Auria & Martini, 2009), while LP tremor is associated with a shallower source close to the eruptive vent, hence more closely related to the explosive mechanism. As a result, the ratio between LP and VLP best indicates significant shifts in the eruptive style, which, for the Tajogaite eruption have principally occurred between LU1 and LU2 (24–28 September) and between the MU and the UU (25–27 November) (Figure 5b). In particular, the volcanic tremor decreases significantly for a few hours on September 27 to start again during the sedimentation of LU2; a clear decrease in VLP amplitude is also shown between the sedimentation of MU2–5 and MU6 (2 November) even though this is less evident from the ratio of the LP/VLP amplitude (Figure 5a). LU1 is also associated with the first peak in TADR that decreases just after the collapse of the cone on 25 September (Romero et al., 2022a); the largest values of TADR are observed just after the beginning of LU2 and tend to stabilize during the MU and decrease in association with the large plumes produced on 12–13 December (final climactic phase occurred during sedimentation of UU2) (Figure 5c).

### 4.3. Spatial Distribution, Volume, and MER of the Tephra Blanket

The overall tephra blanket NE of the vents thins faster than the tephra blanket SW of the vents, with the population of the largest scoria clasts at the most proximal locations (LP27 and LP35, respectively) being also finer (Figures 4b–4d). All investigated layers and units as well as the total deposit are elongated NE-SW and equally distributed NE and SW, with only UU being slightly more dispersed toward SW and the layer MU1 being more dispersed toward SSW (Figures 6 and 7). Values of thickness of excavated trenches vary between about 0.6 and 190 cm (Figure 4; Table S1 in Supporting Information S1). As discussed above, tephra was mostly produced from the southern vents (red vents in Figures 1, 6, and 7). Values of deposit bulk density increase with distance from the vent for the total deposit and the three units (Figure 7e). In fact, they vary between 634 and 1,335 kg m<sup>-3</sup> for layers of the LU (LU1, LU2, and LU3), between 906 and 1,743 kg m<sup>-3</sup> for layers of the MU and between 970 kg m<sup>-3</sup> and 1,491 kg m<sup>-3</sup> for the UU (Figure 7e). In order to obtain unbiased values, mean bulk deposit density for LU, MU, UU, and total deposit was determined from cumulative samples (circles in Figure 7e). Samples of LU seem to show a lower density than samples of MU and UU, being mostly associated with values <1,200 kg m<sup>-3</sup>.

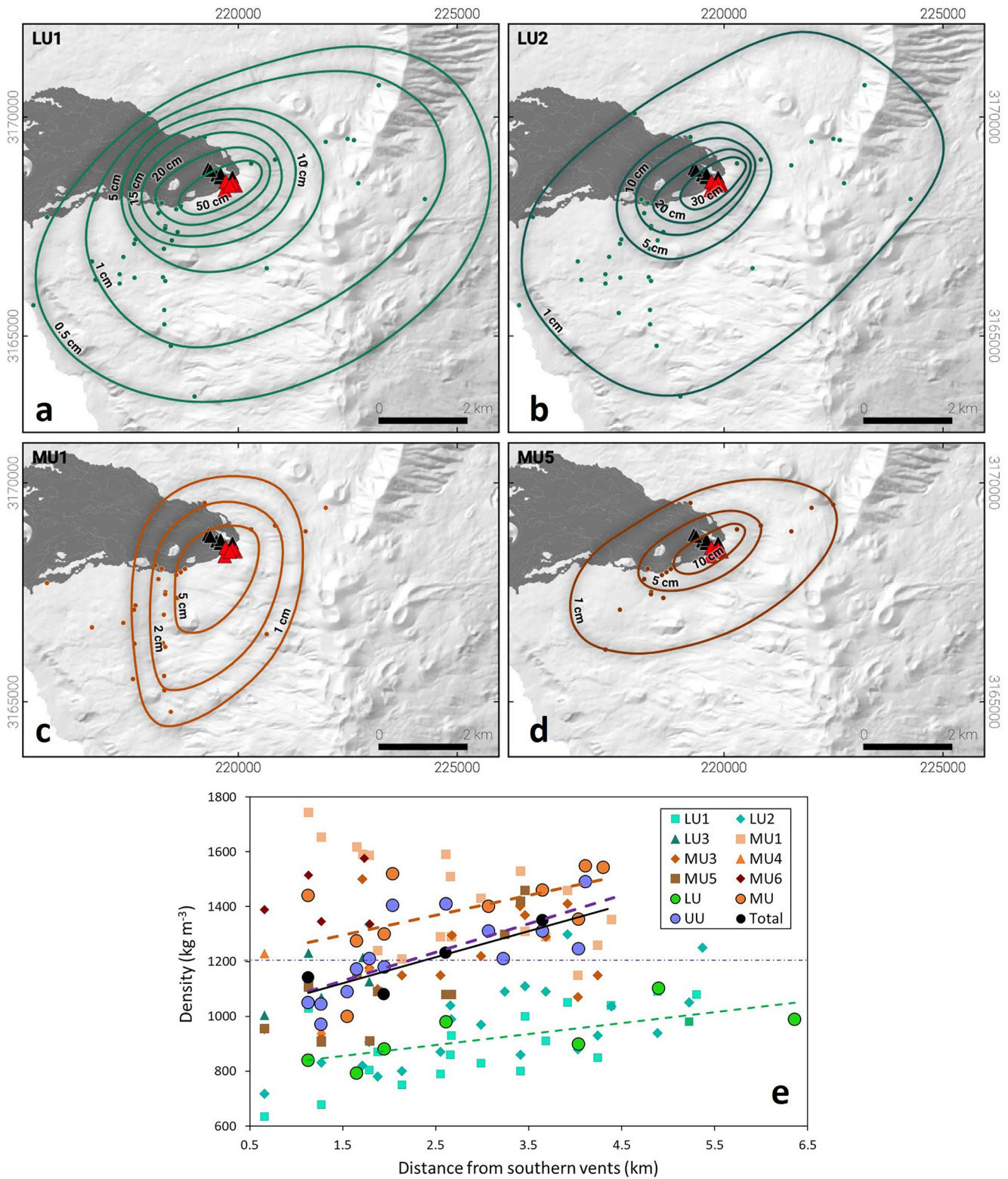
Most layers, all units as well as the total tephra blanket show at least two exponential segments in semilog plots of deposit thickness versus square root of isopach contour, with the only exception of layers MU1 and MU5 (Table 1 and Figure A1 in Appendix A). Given the poor exposure of some of the layers and sublayers that results in a small number of isopach contours within a short range of values of square root of areas, the exponential fit is sometimes associated with only 1 segment (MU1 and MU5), while the Weibull fit could only be made stable using recommended values of  $\theta$  and  $\lambda$  as suggested by Bonadonna and Costa (2013) for different VEIs. In contrast, results obtained from the power law integration are more stable and the sum of the volume of LU, MU, and UU ( $2.2 \times 10^7$  m<sup>3</sup>) well agrees with the volume of the total tephra blanket as calculated from the power law ( $2.3 \times 10^7$  m<sup>3</sup>). We therefore consider the power law as the most reliable method for this tephra blanket and focus on this method in the analyses thereafter. Similarly, we report the volume, and all subsequent values computed from the volume, as the median and the 90% confidence interval (see Section 3 and Supporting Information S1 for associated uncertainty analysis). Volumes of individual layers (as calculated based on the power law fit) vary between  $1.3 \pm 0.2 \times 10^6$  m<sup>3</sup> (MU1) and  $4.9 \pm 0.7 \times 10^6$  m<sup>3</sup> (LU2), while volumes of individual units vary between  $4.5 \pm 0.8 \times 10^6$  m<sup>3</sup> (UU) and  $9.2 \pm 0.6 \times 10^6$  m<sup>3</sup> (LU) (Table 1). The LU is, therefore, the most voluminous unit. Values of bulk deposit density have been used to convert volumes to erupted mass as well as MER based on durations (Tables 2 and 3). Values of MER (as derived from the power law integration of the tephra blanket) vary between  $4.4 \pm 1.2 \times 10^3$  kg s<sup>-1</sup> (LU2) and  $5.8 \pm 1.8 \times 10^3$  kg s<sup>-1</sup> (LU1) for individual layers and  $2.7 \pm 0.6 \times 10^3$  kg s<sup>-1</sup> (MU) and  $4.3 \pm 0.8 \times 10^3$  kg s<sup>-1</sup> (LU) for individual units. When calculated using the total tephra blanket, the average MER for the whole eruption is  $3.7 \pm 0.6 \times 10^3$  kg s<sup>-1</sup> (Table 3).



**Figure 6.** Isopach maps of (a) total deposit, (b) Lower Unit (LU), (c) Middle Unit (MU), and (d) Upper Unit (UU). Inundated area of lava flow (dark gray area) as well as eruptive vents (black and red triangles being the vents mostly producing lava and tephra, respectively) are shown. Thickness values (in cm) of each contour are indicated, while thickness values of individual locations are in Table S1 in Supporting Information S1. Color of contours correlates with colors of Figure 3.

#### 4.4. Eruption Dynamics and Classification

Thinning of tephra blanket of the whole eruption as well as that of individual units and selected layers plot above the Strombolian paroxysms of Stromboli and Etna volcanoes and in between the thinning of the tephra blanket associated with the 1992 eruption of Cerro Negro (Nicaragua) and the 1998 eruption of Etna (Italy), which have been classified as sub-Plinian; other long-lasting hybrid eruptions plot both below (Mirador 1979, Chile) and above (Parícutin 1943–1952 and El Jorullo 1759–1774, Mexico; Navidad-Lonquimay 1988–1990, Chile) the 2021 Tajogaite eruption depending on their duration (Figure 8a). In fact, the thinning plot often used to classify volcanic eruptions (e.g., Alfano et al., 2011, 2018; Houghton et al., 2000; Rowland et al., 2009) can be misleading when comparing eruptions with significantly different durations. When normalizing the values of thickness based on the duration expressed as number of days (Figure 8b; Table 3 and Table S5 in Supporting Information S1),



**Figure 7.** Isopach maps of (a) layers LU1 and (b) LU2 of Lower Unit (LU) and of (c) layers MU1 and (d) MU5 of Middle Unit (MU). Inundated area of lava flow (dark gray area) as well as eruptive vents (black and red triangles being the vents mostly producing lava and tephra, respectively) are shown. Thickness values (in cm) of each contour are indicated, while thickness values of individual locations are in Table S1 in Supporting Information S1. Color of contours correlates with colors of Figure 3. (e) Variation of deposit density with distance from southern vents. Dashed horizontal black line separates most samples of LU (green symbols) from samples of MU (orange to brown symbols) (same color code as in Figure 3). Trend lines for LU (dashed green), MU (dashed brown), UU (dashed violet), and total deposit (black) are also shown.

**Table 1**

*Volumes of Individual Layers, Individual Units, and Total Tephra Blanket Based on Exponential (With 1, 2, and 3 Segments), Power Law, and Weibull Integrations Expressed as the Median ± the 90% Confidence Interval*

	Volume ( $\times 10^6$ m <sup>3</sup> )				
	Exponential			Power law (exp)	Weibull
	1 seg.	2 seg. (BS)	3 seg. (BS1, BS2)		
LU	—	7.8 ± 0.5 (3.9)	7.9 ± 0.5 (3.1, 4.2)	9.2 ± 0.6 (2.1)	6.5 ± 0.3
LU1	3.3 ± 0.2	4.0 ± 0.5 (1.9)	4.0 ± 0.4 (1.7, 6.0)	4.4 ± 0.5 (2.5)	4.2 ± 0.3
LU2	—	2.8 ± 0.2 (2.8)	—	4.9 ± 0.7 (1.8)	3.0 ± 0.2
MU	—	6.5 ± 0.5 (2.7)	6.1 ± 1.0 (2.1, 2.6)	7.8 ± 1.1 (2.1)	6.0 ± 0.3
MU1	0.7 ± 0.1	—	—	1.3 ± 0.2 (1.9)	0.8 ± 3.4
MU5	0.7 ± 0.1	—	—	1.8 ± 0.4 (1.7)	0.8 ± 0.1
UU	—	2.4 ± 0.1 (3.0)	2.6 ± 0.2 (1.9, 6.4)	4.5 ± 0.8 (1.7)	2.6 ± 0.1
Total	—	17.5 ± 0.9 (3.4)	17.5 ± 0.9 (3.5, 4.4)	22.8 ± 1.7 (2.0)	25.0 ± 7.0

*Note.* Values of break in slope for the 2-segment (BS) and 3-segment (BS1, BS2) exponential fit (in km) and the power law exponent (exp) are indicated in brackets. For the power law, the uncertainty on the distal integration limit is bounded by the square root of the area of the of 0.1 and 0.01 cm isopach which correspond to 30 and 90 km for LU, 15 and 45 km for LU1, 30 and 100 km for LU2, 30 and 80 km for MU, 15 and 50 km for MU1, 20 and 70 km for MU5, 25 and 100 km for UU, and 60 and 150 km for the total deposit. See also Tables S2 and S3 in Supporting Information S1 for details on full uncertainty analysis.

clearly the 1886 Plinian eruption of Tarawera (New Zealand) plots above the sub-Plinian eruptions of Cerro Negro 1992 (Nicaragua), Etna 1998 (Italy), and Fuego 1974 (Guatemala), while all long-lasting, hybrid eruptions plot together with normal Strombolian eruptions (Figure 8b). While the duration of the different events considered in this analysis is affected by large uncertainty (Table S5 in Supporting Information S1), Figure 8 clearly demonstrates the complexity of describing and classifying eruptions with significantly different durations (from a few minutes to a few years). Here, below, we investigate a combination of alternative strategies that can help better understand the dynamics of long-lasting, hybrid eruptions considering all associated products (tephra blanket, tephra cone, lava flows).

The beginning of the Tajogaite eruption on 19 September 2021 was characterized by simultaneous effusive and explosive activity. As a result, while the lava flow started descending toward the ocean on the west side of the island, a new cone started forming in the area of Cabeza de Vaca. The new cone went through various

**Table 2**

*Mass of Individual Layers, Individual Units, and Total Tephra Blanket Calculated From Values of Volume (Table 1) and Values of Deposit Density (Figure 7e)*

	Mass ( $\times 10^9$ kg)					
	Deposit density (kg m <sup>-3</sup> )	Exponential			Power law	Weibull
		1 seg.	2 seg.	3 seg.		
LU	926 ± 93	—	7.3 ± 1.2	7.3 ± 1.3	8.5 ± 1.5	6.0 ± 1.0
LU1	891 ± 89	3.0 ± 0.5	3.6 ± 0.8	3.6 ± 0.7	4.0 ± 0.8	3.7 ± 0.7
LU2	982 ± 98	—	2.8 ± 0.6	—	4.9 ± 1.1	2.9 ± 0.5
MU	1,386 ± 137	—	9.0 ± 1.7	8.5 ± 2.0	10.8 ± 2.4	8.4 ± 1.5
MU1	1,416 ± 142	1.1 ± 0.2	—	—	1.8 ± 0.5	1.2 ± 4.7
MU5	1,133 ± 113	0.8 ± 0.2	—	—	2.0 ± 0.5	0.9 ± 0.2
UU	1,221 ± 122	—	3.0 ± 0.5	3.2 ± 0.6	5.4 ± 1.2	3.1 ± 0.5
Total	1,200 ± 120	—	20.9 ± 3.8	20.9 ± 3.8	27.2 ± 4.8	30.0 ± 9.7

*Note.* See also Tables S2 and S3 in Supporting Information S1 for details on full uncertainty analysis.



**Table 3**  
Mass Eruption Rate Derived From Mass of Erupted Tephra (as Calculated From the Integration of the Power Law Trend) (Table 2) and Duration

	Duration (days)	Duration ( $\times 10^6$ s)	Type 1 winds	Type 2 winds	Mass eruption rate ( $\times 10^3$ kg $s^{-1}$ ) (power law)
LU	23 $\pm$ 1	2.0 $\pm$ 0.1	7 (*)	11 (*)	4.3 $\pm$ 0.8
LU1	8 $\pm$ 2	0.7 $\pm$ 0.2	0 (*)	3 $\pm$ 2 (*)	5.8 $\pm$ 1.8
LU2	13 $\pm$ 2	1.1 $\pm$ 0.2	6 $\pm$ 1	7 $\pm$ 1	4.4 $\pm$ 1.2
MU	46 $\pm$ 2	4.0 $\pm$ 0.2	24 $\pm$ 2	22 $\pm$ 2	2.7 $\pm$ 0.6
MU1	4 $\pm$ 2	0.3 $\pm$ 0.2	3 $\pm$ 1	1 $\pm$ 0	5.3 $\pm$ 3.3
UU	17 $\pm$ 1	1.5 $\pm$ 0.1	14 $\pm$ 1	3 $\pm$ 1	3.7 $\pm$ 0.9
Total	86	7.4	46	36	3.7 $\pm$ 0.6

Note. Duration of individual layers and units was derived based on direct observations (Figure S1 in Supporting Information S1), but it is not available for MU5 (Figure 5). Uncertainty of 1 day for Lower Unit (LU) and Upper Unit (UU) and of 2 days for the remaining layers and units is considered in the calculation of mass eruption rate (MER). See Tables S2 and S3 in Supporting Information S1 for details on full uncertainty analysis. Number of days characterized by trade winds (Type 1) and when trade winds are weak or inexistent (Type 2) are also shown (see also Figure 2). (\*): indicates that data set is not complete.

partial collapses reaching a height of about 110 m above the pre-eruptive surface on 27 September and of 187 m at the end of the eruption (Civico et al., 2022a, 2022b). On 25 September, an increase in the magmatic input, resulting in increased fountaining intensity, caused a large partial collapse of the cone (Romero et al., 2022a). This partial collapse coincided with the end of sedimentation of layer LU1 and with an increase in the lava flow emission (Figure 9). A sharp increase in the emission rate of lava flows occurred after the first week of the eruption (after the sedimentation of LU1); in contrast, the MER associated with the cone and the tephra blanket remained relatively constant during the whole eruption (Figures 5c and 9 and Tables 3 and 4). In fact, at the end of sedimentation of layer LU1, the erupted mass of lava ( $2.6 \times 10^{10}$  kg) was more than double the mass of tephra constituting the cone ( $7.1 \times 10^9$  kg) and about 1 order of magnitude larger than the mass of the tephra blanket ( $4.0 \times 10^9$  kg) (Figure 9 and Table 4). Between 25 and 30 September 2021 (beginning of LU2), the emission of lava increased from  $1.9 \times 10^4$  to  $1.5 \times 10^5$  kg  $s^{-1}$  (i.e., from 7 to 55  $m^3 s^{-1}$ ; Figure 5c). As a result, at the end of sedimentation of LU, the mass of lava ( $1.5 \times 10^{11}$  kg) was 1 order of magnitude larger than the cone ( $9.9 \times 10^9$  kg) and the tephra blanket ( $8.5 \times 10^9$  kg) (Table 4). At the end of the eruption, the mass of lava ( $4.8 \times 10^{11}$  kg) was also 1 order of magnitude larger than the cone ( $4.2 \times 10^{10}$  kg) and the tephra blanket ( $2.7 \times 10^{10}$  kg) (Table 4). It is important to stress that only the subaerial lava is considered in this analysis, and, therefore, the total volume (also considering the submarine lava) would be even larger. The density of the lava flow was taken as  $2,770$  kg  $m^{-3}$  based on compositional data, while the density of the cone was considered as that

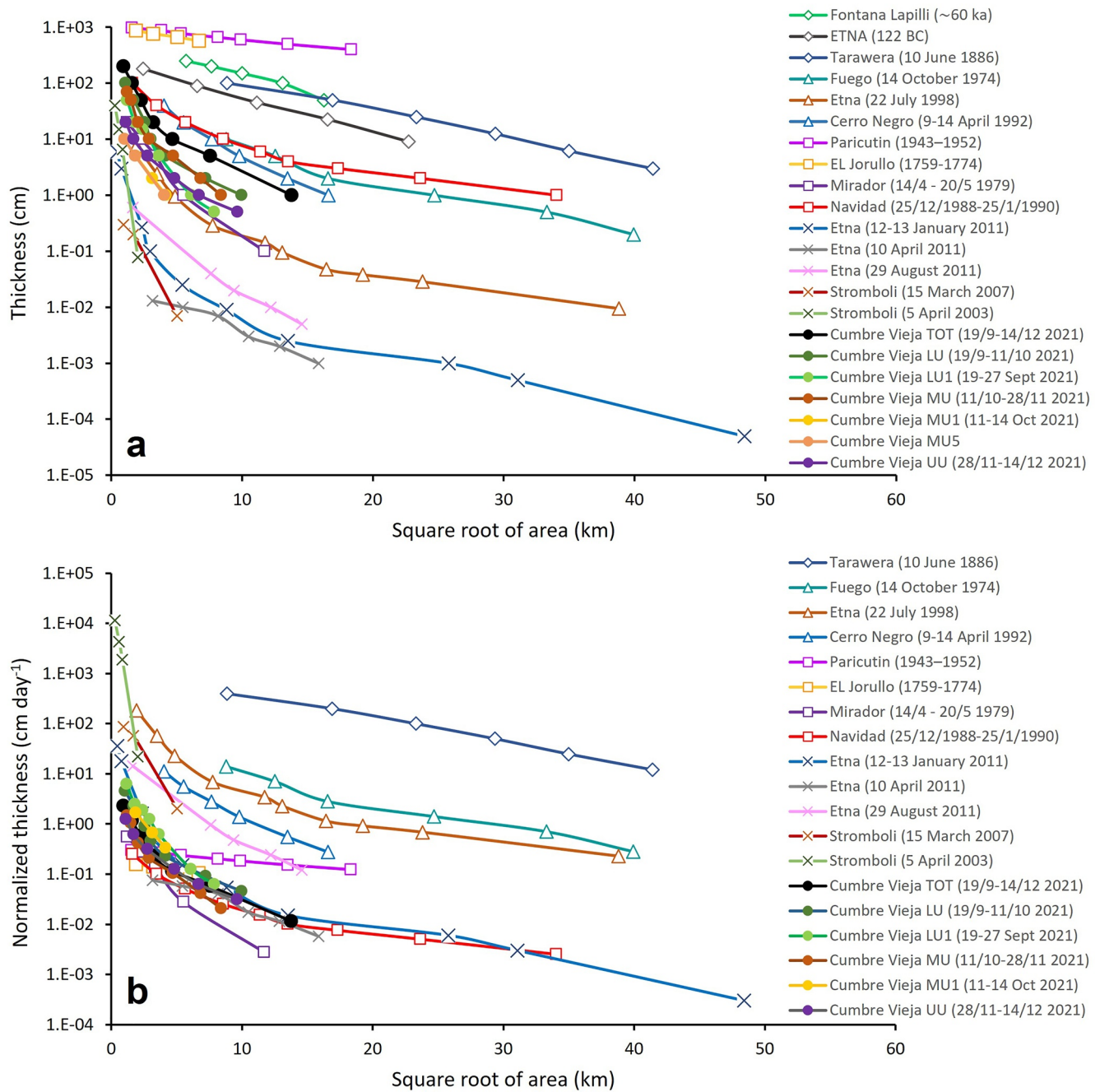
of the proximal tephra blanket (<1.5 km from vents; see caption of Table 4 for details). Finally, even though the volume of the cone was accurately determined based on UAS survey only on 27 September 2021 and January 2022 (end of sedimentation of layer LU1 and of UU, respectively; Civico et al., 2022a, 2022b), it was extrapolated for the LU and the MU based on the linear fit shown in Figure 9 (for the mean, the minimum, and maximum values).

All units, layer LU1 and the total Tajogaite eruption plot together with other hybrid eruptions in the Magnitude Index versus Intensity Index plot proposed by Pyle (2000) (where the Magnitude Index is calculated based on the combination of tephra blanket, tephra cone, and lava flow); nonetheless, unlike the Parícutin eruption that shows an increase of MER in time, the MER of the Tajogaite eruption remained relatively constant in time (Figure 10a and Table 4). The ratio between the mass of the tephra blanket and the total mass (cumulative mass of tephra blanket, cone, and lava) used often as a proxy for eruption explosivity (Pioli et al., 2009), is 0.05, 0.04, and 0.07 for LU, MU, and UU, respectively (when the mean value of cone and lava volume is considered). This indicates, together with a cumulative MER of tephra blanket, cone, and lava  $<10^5$  kg  $s^{-1}$  (Table 4), a clear dominance of the effusive component of the eruption; the same ratio is 0.11 for LU1 (the highest of the eruption) and 0.05 for the whole eruption (Figure 10b). The Tajogaite eruption plots in the field of decoupled magma-gas systems even when considering the minimum and maximum values of cone and lava volume as shown in Figure 9 (Figure S10 in Supporting Information S1).

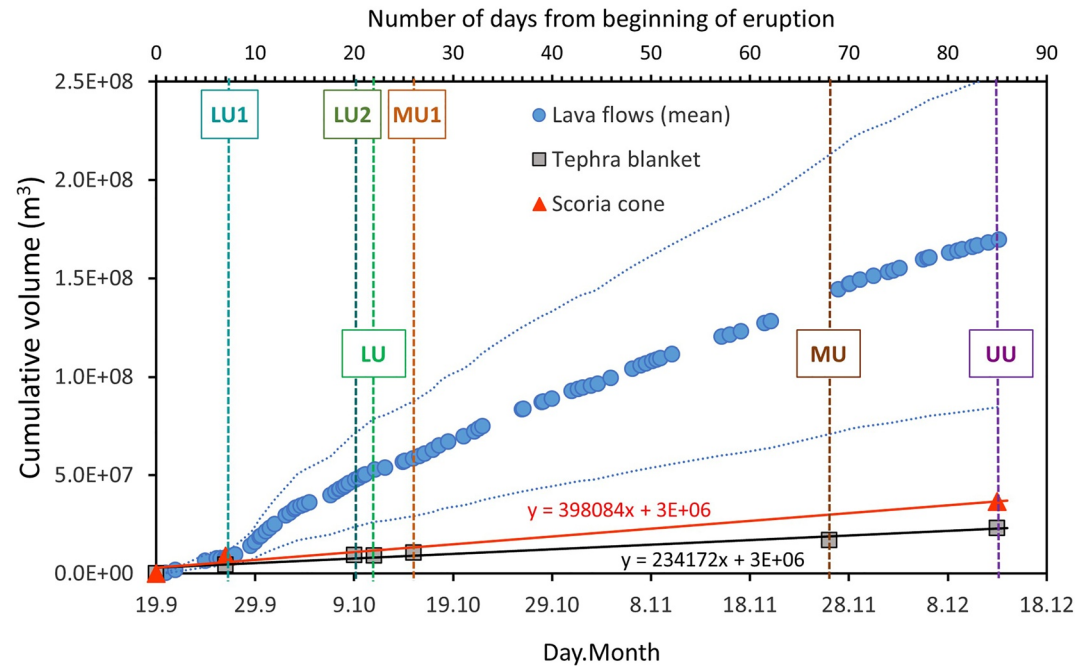
## 5. Discussion

### 5.1. Characteristics of the Tephra Blanket Associated With the 2021 Tajogaite Eruption

Even though the tephra blanket does not represent the dominant component of the 2021 Tajogaite eruption, which was clearly associated with a magma-gas decoupled system (Figure 10b), it impacted most of the south section of the island dispersing tephra both SW and NE of the vents (Figures 6 and 7). In addition, the stratigraphic characteristics as well as the size and texture of clasts in the different units and layers represent a clear indication of the shift in eruptive style and dynamics through the whole activity. Vents opened at different times resulting in specific eruptive phases with different characteristics. As an example, the opening of a new vent on 13–15 October 2021 was associated with the sedimentation of a distinctive layer of red lithic clasts



**Figure 8.** Comparison of thinning of tephra blanket of basaltic eruptions of different intensity considering (a) the values of thickness (in cm) and (b) the values of thickness normalized based on the eruption duration expressed in number of days (only for the eruption for which the duration is observed; Table 3 and Table S5 in Supporting Information S1) (in  $\text{cm day}^{-1}$ ). Plinian eruptions: indicated with the diamond symbols (Fontana Lapilli: Costantini et al., 2009; Etna 122 B.C.: Coltelli et al., 1998; Tarawera 1886: Houghton et al., 2004); sub-Plinian eruptions: indicated with the triangle symbols (Cerro Negro 1992: Connor & Connor, 2006; Fuego 1974: Rose et al., 2008; Etna 1998: Scollo et al., 2013); hybrid long-lasting eruptions: indicated with square symbols (Paricutin 1943–1952 and El Jorullo 1759–1774: Rowland et al., 2009; Navidad-Lonquimay 1988–1990: Naranjo et al., 1991; Mirador 1979: Moreno, 1980) and Strombolian paroxysms: indicated with cross symbols (Etna 12–13 January 2011: Andronico et al., 2014; Etna 10 April 2011: Freret-Logeril et al., 2021a; Etna 29 August 2011: Freret-Logeril et al., 2021b; Stromboli 5 April 2003 and 15 March 2007; Pistolesi et al., 2011). Total tephra blanket, units, and selected layers of the 2021 Tajogaite eruption are indicated with filled circles of various colors. Durations of all eruptions are indicated in legend (duration of MU5 layer is not indicated as it is not constrained; Figure 5). Points are visualized as scatter plots with smooth lines to best identify the different eruptions.



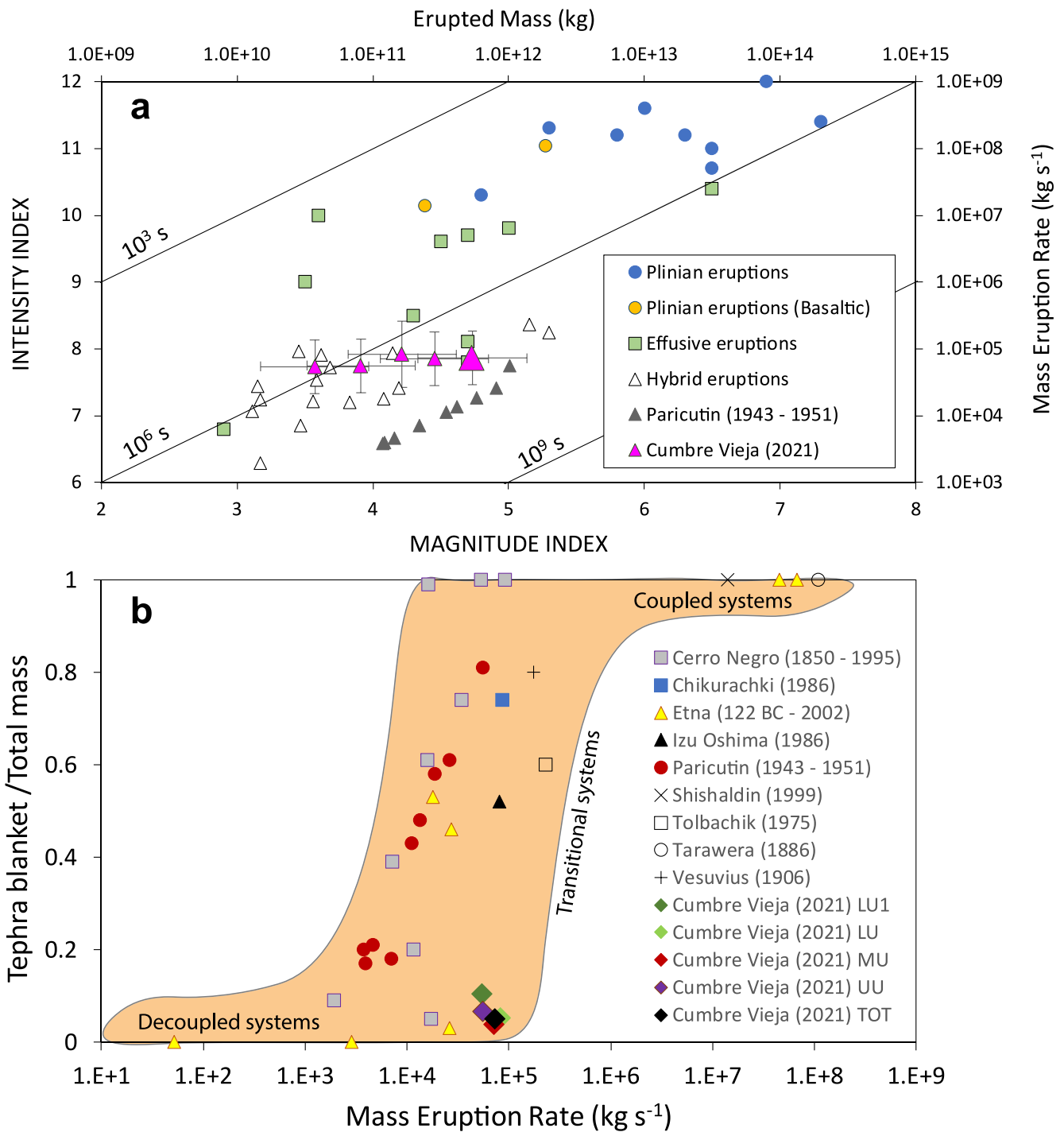
**Figure 9.** Variation in time of volume ( $\text{m}^3$ ) associated with lava flows (mean value: blue circles; minimum and maximum values: blue dotted lines), tephra cone (as determined based on UAS surveys; Civico et al., 2022a, 2022b; red triangles), and tephra blanket (as determined from isopach maps of Figures 6 and 7; gray squares). A linear fit and associated equation are shown for the cone and the tephra blanket data sets where  $x$  represents the number of days from the beginning of the eruption (secondary horizontal axis). Vertical dashed lines indicate the best guess of the end of individual units and selected layers (as shown in Figure 5 and Figure S1 in Supporting Information S1).

**Table 4**

*Erupted Mass and Mass Eruption Rate for the Total Eruption, the Three Units, and LU1 Associated With Tephra Blanket, Scoria Cone, and Lava Flow*

	Erupted mass tephra blanket (PL) ( $\times 10^{10}$ kg)	Erupted mass tephra cone ( $\times 10^{10}$ kg)	Erupted mass lava ( $\times 10^{10}$ kg)	Total erupted mass ( $\times 10^{10}$ kg)	Magnitude Index
LU	$0.8 \pm 0.15$	$1.0 \pm 0.005$	$14.6 \pm 7.3$	$16.4 \pm 7.3$	$4.2 \pm 0.4$
LU1	$0.4 \pm 0.08$	$0.7 \pm 0.015$	$2.6 \pm 1.3$	$3.7 \pm 1.3$	$3.6 \pm 0.4$
MU	$1.1 \pm 0.24$	$2.0 \pm 0.013$	$25.4 \pm 12.7$	$28.5 \pm 12.7$	$4.5 \pm 0.4$
UU	$0.5 \pm 0.12$	$0.7 \pm 0.013$	$7.0 \pm 3.5$	$8.2 \pm 3.5$	$3.9 \pm 0.4$
Total	$2.7 \pm 0.48$	$4.2 \pm 0.034$	$47.8 \pm 23.5$	$54.7 \pm 23.9$	$4.7 \pm 0.4$
	MER tephra blanket (PL)( $\times 10^4$ kg $\text{s}^{-1}$ )	MER tephra cone ( $\times 10^4$ kg $\text{s}^{-1}$ )	MER lava ( $\times 10^4$ kg $\text{s}^{-1}$ )	Total MER ( $\times 10^4$ kg $\text{s}^{-1}$ )	Intensity Index
LU	$0.4 \pm 0.08$	$0.5 \pm 0.002$	$7.3 \pm 3.8$	$8.2 \pm 3.8$	$7.9 \pm 0.5$
LU1	$0.6 \pm 0.16$	$1.0 \pm 0.023$	$3.8 \pm 1.9$	$5.4 \pm 1.9$	$7.7 \pm 0.4$
MU	$0.3 \pm 0.06$	$0.5 \pm 0.003$	$6.4 \pm 3.2$	$7.2 \pm 3.2$	$7.9 \pm 0.4$
UU	$0.4 \pm 0.09$	$0.5 \pm 0.008$	$4.8 \pm 2.4$	$5.7 \pm 2.4$	$7.7 \pm 0.4$
Total	$0.4 \pm 0.06$	$0.6 \pm 0.005$	$6.3 \pm 3.2$	$7.3 \pm 3.2$	$7.9 \pm 0.4$

*Note.* Magnitude Index and Intensity Index of Pyle (2000) for the cumulative erupted mass and mass eruption rate (MER) including tephra blanket, scoria cone, and lava flows are also shown. See Tables 2 and 3 for erupted mass and MER of tephra blanket (value obtained from the Power Law integration). Uncertainty on the determination of volume of cone ( $\pm 0.3 \times 10^6 \text{ m}^3$  on the final value and  $\pm 0.2 \times 10^6 \text{ m}^3$  on the value for the 27 September 2022) are from Civico et al. (2022a). Volume of tephra cone at different times of the eruptions was extrapolated from linear fit of Figure 9 and converted into mass based on values of density of 798, 840, 1,080, 1,037, and 1,140  $\text{kg m}^{-3}$  for LU1, LU, MU, UU, and total deposit, respectively, averaged for associated locations  $< 1.5$  km from vents (see Figure 7e). See also Table S4 in Supporting Information S1 for details on full uncertainty analysis and propagation.



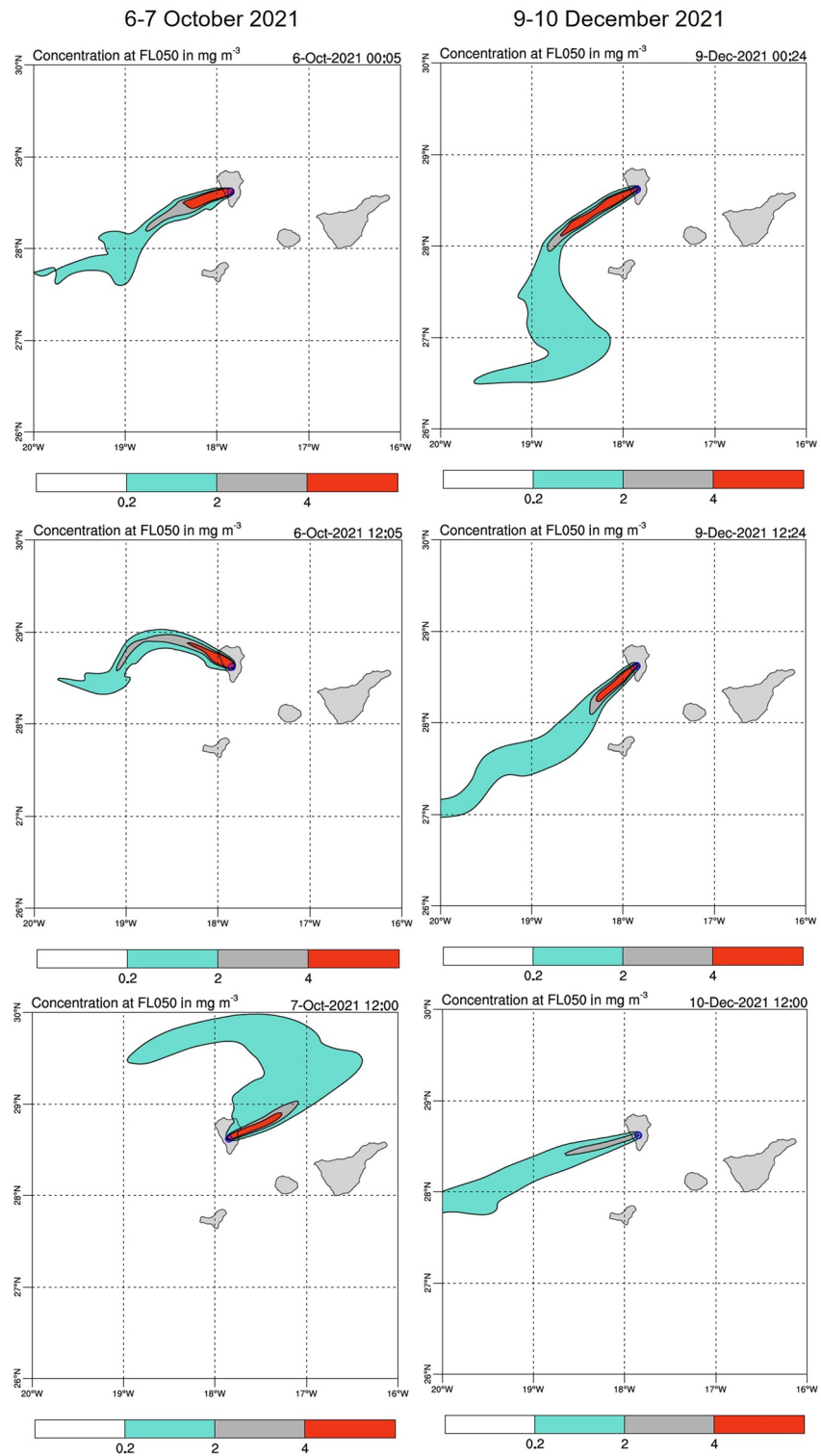
**Figure 10.** (a) Plot of Cumulative Magnitude Index versus Cumulative Intensity Index of Pyle (2000) (corresponding values of erupted mass and mass eruption rate (MER) are also shown on secondary axis); diagonal lines indicate the eruption duration given a certain Magnitude Index, where  $10^6$  s correspond to about 12 days. Data source: Plinian and effusive eruptions (Pyle, 2000), hybrid eruptions (Pioli et al., 2009). Large pink triangle indicates the whole 2021 Tajogaite eruption; small pink triangles indicate LU1, Upper Unit (UU), Lower Unit (LU), and Middle Unit (MU) from left to right, respectively (error bars indicate associated uncertainty; Table 4). (b) Plot of cumulative MER ( $\text{kg s}^{-1}$ ) (lava, tephra cone, and tephra blanket) versus eruption explosivity indicated as the ratio between the mass of tephra blanket and the total erupted mass (i.e., lava, tephra cone, and tephra blanket) (adjusted from Pioli et al. (2009)). Values of LU, MU, and UU as well as LU1 and total deposit are plotted as diamonds together with the data set of basaltic eruptions from Pioli et al. (2009). See also Table 4 for values of mass and MER for the different eruptive phases and Figure S10 in Supporting Information S1 for plots considering the minimum and the maximum values of total mass.

(MU2; Figure 3). Even though all sublayers, layers, and units were produced by mixed explosive activity including lava fountains, ash emissions, and tephra plumes from four main vents (Figure 1), the stratigraphy analyzed between about 0.7 and 12 km from vents is striking; in fact, sublayers and layers can be well correlated in the proximal and medial deposit (<5 km from vents), while all units are still recognizable also in medial and distal area (>5 km from vents) (Figure 4). Despite plume height varying during the day due to variable eruptive style and wind speed, the MER as derived from tephra blanket was relatively constant during the whole eruption, with an average of  $3.7 \pm 0.6 \times 10^3 \text{ kg s}^{-1}$  for the whole tephra blanket (Figure 9 and Table 3). The 50th percentile of the 20 largest scoria clasts also only varied between 1.4 and 1.9 cm at LP35 (SW of the vent) and between 1.3 and 1.9 cm at LP27 (NE of the vent), indicating similar maximum plume height associated with the different sublayers and layers (Figure 4). The whole population of the 20 largest scoria clasts at locations LP35 and LP27 also show very similar trends with those at LP35 being only slightly coarser than those at LP27 for the same sublayers and layers (Figure 4). In contrast, the density of the deposit is different for the whole LU (mostly  $<1,200 \text{ kg m}^{-3}$ ) with respect to the rest of the stratigraphy (mostly  $>1,200 \text{ kg m}^{-3}$ ) reflecting also the highest 50th percentile of the 20 largest scoria clasts (1.9 cm; Figure 4) and the highest explosivity index (0.11 for LU1; Figure 10b). The UU, which is associated with the highest explosivity index amongst the three units (0.07; Figure 10b), is also characterized by values of deposit density  $<1,200 \text{ kg m}^{-3}$  for distances from the vent  $<2 \text{ km}$  (Figure 7e).

While the tephra was dispersed over the whole island even reaching the Roque de los Muchachos Observatory (about 16 km north of the vents), the associated cumulative deposit shows a clear elongation NE-SW. In fact, not only the cumulative deposit is dispersed in both directions, but all the individual units and most layers have the same dispersal NE-SW, with the only exception for the MU1 layer that is mostly dispersed to SSW (Figures 6 and 7). As an example, LP35 and LP27 (about 1 km SW and NE from the vents, respectively) are nearly specular, showing the same sequence of units, layers, and sublayers with very similar values of thickness (Figure 4 and Table S1 in Supporting Information S1). This indicates that the variations of wind direction are associated with smaller temporal scales than the duration of individual units and layers, which is between 17–46 and 4–13 days, respectively (Table 3). In terms of atmospheric circulation, all units have similar number of days characterized by trade winds (Type 1 in Figure 2; Table 3) and days during which trade winds were weak or inexistent (Type 2 in Figure 2; Table 3). LU and LU1 seem to be characterized by more Type 2 winds because information is only available after 6 days following eruption onset. MU1 is dominated by Type 1 winds, and, in fact, differently from the dispersal of all other layers, the associated tephra blanket is mostly distributed SSW (Figure 7). During days with weak or inexistent trade winds (Type 2), the dispersal of tephra strongly oscillated, even experiencing 360-degree veering, as occurred on 6 October (during sedimentation of LU2; Figure 11). In contrast, during days of trade winds the direction was mostly SW, as shown for 9 December (during sedimentation of UU; Figure 11). Finally, as expected from buoyant plume theory (e.g., Degruyter & Bonadonna, 2012, 2013; Michaud-Dubuy et al., 2020; Woodhouse et al., 2013), the variations in plume height (Figure 2) seem to be dominated more by the characteristics of wind rather than by the short-term MER oscillations. This is suggested by the fact that deposit-derived MER for the tephra blanket is relatively constant across all units and layers (Table 3) and that a clear correlation is observed between wind type and plume height. In fact, Type 1 winds are strong and typically cause plume to bend over resulting in an overall decrease of plume height. In contrast, plumes are more likely to rise vertically during days characterized by Type 2 winds (Figure 2). In fact, even though the plume height varied during the day, while the available data sets provide only one observation per day (PEVOLCA) or every few days (VONA), for both data sets the average plume height is 2.8 km a.s.l. during days characterized by strong trade winds (Type 1) and 3.7 km a.s.l. during days characterized by weak winds (Type 2) (Figure 2). In addition, the highest plume of 8.5 km a.s.l. was observed in the afternoon of 13 December, which was characterized by Type 2 wind.

## 5.2. Implications for Tephra Dispersal Forecasting

The isopach maps of the total deposit as well as the isopach maps of individual layers and units can be described as subcircular to elliptical as they represent the contribution of tephra sedimentation over few days to weeks (Figures 6 and 7). Long-term hazard assessment that would also consider ground sedimentation over a few days to weeks would not need to capture the hourly variation of ESPs (see e.g., the hazard assessment of long-lasting eruptions such as Mt. Etna (Italy) and La Fossa volcano, Vulcano (Italy); Biass et al., 2016; Scollo et al., 2013).



**Figure 11.** Examples from the operational forecast system run at the Barcelona Supercomputing Center (BSC) showing concentration of volcanic ash ( $\text{mg m}^{-3}$ ) at Flight Level FL050 ( $\sim 1,500$  m a.s.l.). The left and right plots show typical plume dispersal during days of wind Type 2 and Type 1, respectively. Zoom of the computational domain centered on La Palma Island. Left column: results for 6 October at 00:00, 6 October at 12:00, and 7 October at 12:00. Right column: results for 9 December at 00:00, 9 December at 12:25, and 10 December at 12:00. Simulations considered volcanic ash only (i.e., tephra particles  $< 2$  mm in diameter). See Supporting Information S1 for the animated full record of these simulations.

Nonetheless, atmospheric tephra dispersal over shorter time scales (e.g., hours), which are of particular interest for real-time forecasting and mitigation of risk to aviation, is more complex (Figure 11 and Movies S1 and S2). From 25 September 2021 onwards, an operational forecast system was implemented at the Barcelona Supercomputing Center (BSC) to deliver daily plume dispersal and tephra fallout predictions to the scientific committee of the PEVOLCA. The modeling system, based on the FALL3D dispersal model (Folch et al., 2020) configured at 2 km resolution, was used as a complement to the Toulouse VAAC forecasts in operational decision making. As an example, Figure 11 shows FALL3D model concentration snapshots at different instants during typical Type 1 (9–10 December) and Type 2 (6–7 October) wind situations. These operational systems provided an accurate and valuable information for the long-range plume dispersal, with overall good agreement with satellite imagery. However, the Tajogaite eruption demonstrated the complexity of modeling proximal dispersal and deposition in case of long-lasting weak eruptions due to several reasons including variable eruptive style and plume height at scales of a few hours to a few days, complex orographic settings yielding to particular local-scale wind patterns and the presence of hot lava flows able to generate significant thermal convection in the near-source regions. All these aspects had implications on model accuracies in proximal areas, as operational VATDMs are normally configured for more sustained eruption conditions and driven by global or regional scale meteorological models. Improving the accuracy of forecasts for such events requires various implementations such as a rapid and automated assimilation of the frequent variations in eruption conditions (e.g., plume height) and shifts in eruptive style and dynamics, a downscaling of the meteorological drivers to resolve the complex and transient wind patterns observed, and the description of the thermal convection effects caused by the emplacement of hot and widespread lava flows.

### 5.3. Characterization and Classification of Long-Lasting, Cone-Forming Basaltic Eruptions

While the concept of long-lasting eruptions can be tentatively quantified to describe eruptive events having duration from a few days to a few years, the term hybrid is commonly used to define volcanic activity characterized by both effusive (lava flows, lava domes) and explosive products (tephra, scoria cones, pyroclastic density currents) often resulting from variable eruptive styles occurring contemporaneously (e.g., Wadsworth et al., 2020). The variability in style shown by hybrid volcanism can be the result of a complex interplay among magma composition, crystal, and volatile content dissolved in the melt (which all modulate magma rheology and ascent along the conduit) and is associated to magmatism with variable degrees of evolution (i.e., basaltic to rhyolitic activity) (Alfano et al., 2018; Cassidy et al., 2018; Castro & Gardner, 2008; Pioli et al., 2009; Pistolesi et al., 2021; Schipper et al., 2013; Wadsworth et al., 2020; Zawacki et al., 2019). Particularly, basaltic volcanism can be often associated to monogenetic activity which may further enhance hybrid characteristics being associated with relatively immature conduits and low viscosity magma; these two factors may favor splitting into vertical and lateral branches near the base of the forming scoria cone. If the flow is separated, gas and liquid components of the magma may be partitioned unevenly between the two branches, resulting in external dynamics with very different characteristics (Pioli et al., 2009).

The variability in eruptive dynamics of long-lasting, hybrid basaltic eruptions showing significant shifts in eruptive style and a variable ratio between effusive and explosive products results in a complex description and classification. As an example, the basaltic eruption of Tecolote volcano (Mexico) ( $27 \pm 6$  ka) was characterized by a first sub-Plinian phase followed by a violent Strombolian phase and associated with the effusion of a large volume of lava, where the tephra blanket only represents about 23% of the cumulative volume (Zawacki et al., 2019). The 1943–1952 eruption of Parícutin was also associated with multiple eruptive styles including violent Strombolian phases, normal Strombolian explosions, Vulcanian explosions, ash emissions, and effusive phases (Pioli et al., 2008); this resulted in variable ratios of mass of tephra blanket versus total mass (Figure 10). The first year of the eruption was more explosive with plume heights  $\leq 8$  km, wide ash dispersal (up to about 400 km of the volcano), average daily tephra discharge rates of about  $10^5$  kg s<sup>-1</sup> and contemporaneous lava discharge rate of about  $10^4$  kg s<sup>-1</sup>, while the last six years were mostly effusive with short-lived Vulcanian explosions with heights  $\leq 2$  km and MER  $< 10^4$  kg s<sup>-1</sup> (Foshag & González, 1956; Krauskopf, 1948; Ordoñez, 1945; Velasco, 1945). During the Parícutin eruption, effusive and explosive activities were associated with different vents, with the summit vents mostly producing tephra and the vents at the base of the cone mostly producing lava flows. Within a few hours from the beginning of the eruption, a mild explosive activity concentrated in the northern section of the 50-m-long fracture forming

a scoria cone that reached its stability, and final height of 150 m, after about 1 month; similarly to the Navidad eruption of Lonquimay, Chile (1988–1990) (Naranjo et al., 1991), the cone stabilization coincided with the beginning of the violent Strombolian phase with a high production of ash and contemporaneous emission of lava from lateral vents at the base of the cone (Pioli et al., 2009). Variable gas segregation and upward gas migration within the upper conduit caused the magma-gas mixture to alternate between stable and unstable two-phase flow regimes, which in turn gave rise to highly unstable and variable eruptive activity. Such a complexity in eruptive style and dynamics is difficult to be captured in a single plot or a single classification scheme, especially when eruptive duration and the combination of multiple products (e.g., tephra blanket, cone, lava flows) are not considered (e.g., VEI, thinning plot).

The whole Tajogaite eruption is associated with a VEI 3, while all individual units and individual layers analyzed are associated with a VEI 2 (Table 1). In addition, the thinning of the tephra blanket of the whole eruption as well as of individual units and selected layers (LU1, MU1, MU5) show some similarities with sub-Plinian deposits (e.g., Cerro Negro 1992, Nicaragua; Etna 1998, Italy; Fuego 1974, Guatemala; Figure 8a). In fact, the eruptions of Fuego 1974, Cerro Negro 1992, and Etna 1998 lasted <4 days (Table S5 in Supporting Information S1), which is significantly less than all considered units of Tajogaite, with the exception of layers LU1 (8 days) and MU1 (3 days) (Table 3). In addition, the eruption of Fuego 1974, Cerro Negro 1992, and Etna 1998 were associated with absent or small emission of lava flows (Connor & Connor, 2006; Pioli et al., 2009; Rose et al., 2008; Scollo et al., 2013). It is also interesting to notice how the 1943–1952 eruption of Parícutin and the 1759–1774 eruption of El Jorullo (Mexico), both mostly characterized by violent Strombolian activity (Pioli et al., 2008; Rowland et al., 2009), plot above the three Plinian eruptions of Tarawera (New Zealand; Houghton et al., 2004), Fontana Lapilli (Nicaragua; Costantini et al., 2009), and Etna (122 BC; Coltelli et al., 1998), demonstrating the difficult comparison of eruptions with significantly different durations based only on tephra blanket thinning (Figure 8a). When the values of thickness are normalized based on the eruption duration, all long-lasting hybrid eruptions plot below sub-Plinian and Plinian events (Figure 8b). In fact, the classification schemes typically used for short-lasting eruptions, and designed to describe magma-gas coupled systems, do not provide a good description of long-lasting, hybrid eruptions, which are, in fact, typically characterized by variable eruptive style, multiple products, and unsteady activity, with unsteadiness being related to eruption intensity.

Coupled, transitional, and decoupled systems are better described when plotting the Magnitude Index versus the Intensity Index (Figure 10a) as well as the explosivity index (i.e., the ratio between the mass of tephra blanket and the total erupted mass of lava, tephra cone, and tephra blanket) versus MER (Figure 10b). The first scheme clearly discriminates Plinian and effusive eruptions from long-lasting hybrid eruptions that mostly plot beyond the diagonal of  $10^6$  s and identifies eruptions with varying intensity in time (e.g., Tajogaite versus Parícutin; Figure 10a). The MER, and, therefore, the Intensity Index, is also clearly related to the degree of magma-gas decoupling. In particular, according to the numerical simulations of Pioli et al. (2009), low, intermediate, and high values of MER are associated with effusive and normal Strombolian eruptions ( $\text{MER} < 10^3 \text{ kg s}^{-1}$ ; Intensity Index < 6), violent Strombolian eruptions ( $\text{MER} = 10^3\text{--}10^5 \text{ kg s}^{-1}$ ; Intensity Index = 6–8), and sustained sub-Plinian to Plinian activity without accompanying lava flows ( $\text{MER} > 10^5 \text{ kg s}^{-1}$ ; Intensity Index > 8), respectively. The shift in style has been associated with higher values of MER for the 1943–1952 Parícutin eruption (Mexico), where violent Strombolian activity was characterized by values of MER between  $10^4$  and  $10^5 \text{ kg s}^{-1}$  (Intensity Index = 7–8) (Pioli et al., 2008). This is also the case of Vesuvius, with ash emissions and normal Strombolian activity being associated with  $\text{MER} < 10^5 \text{ kg s}^{-1}$  (Intensity Index < 8), violent Strombolian eruptions with  $\text{MER} = 10^5\text{--}10^6 \text{ kg s}^{-1}$  (Intensity Index = 8–9), sub-Plinian eruptions with  $\text{MER} = 10^6\text{--}10^7 \text{ kg s}^{-1}$  (Intensity Index = 9–10), and Plinian eruptions with  $\text{MER} > 10^7 \text{ kg s}^{-1}$  (Intensity Index > 10) (Cioni et al., 2008). These numerical results are not applicable to fissure eruptions, where spatial differentiation of vents is likely related to the dynamics of magma rise within the dike and large MER can be achieved without significant explosive dynamics (Pioli et al., 2009). In addition, similar values of MER can also be associated with Hawaiian lava fountains ( $10^4\text{--}10^5 \text{ kg s}^{-1}$ ), which, however, differ in terms of plume height, components, and glass vesicularity (Mangan & Cashman, 1996; Parfitt, 2004; Pioli et al., 2008; Romero et al., 2018; Wolfe et al., 1988), and intense lava fountains at open conduit volcanoes (e.g., Villarica volcano, Chile; Etna volcano, Italy) ( $\text{MER} = 10^5\text{--}10^6 \text{ kg s}^{-1}$ ; Andronico et al., 2015; Freret-Lorgeril et al., 2018; Romero et al., 2018).



The plot of explosivity versus MER allows also for the contribution of the different components (tephra blanket, cone, and lava) to be described. Interestingly, hybrid eruptions with simultaneous emission of tephra and lava show a direct correlation between explosivity and MER (Pioli et al., 2009; Figure 10b). In particular, decoupled magma-gas systems dominated by effusive activity result in eruptions characterized by a small or nearly absent tephra blanket and low MER, while coupled magma-gas systems are typically associated with sub-Plinian and Plinian activity characterized by a large tephra blanket, nearly absent lava production and large MER; all transitional systems producing a significant tephra blanket as well as substantial lava flows can result in normal Strombolian or violent Strombolian systems (Figure 10b). In fact, scoria cones of similar size (100–300 m) can be associated with both normal Strombolian and violent Strombolian eruptions, with the main difference that violent Strombolian eruptions are also associated with an extended tephra blanket and large volumes of volcanic ash (e.g., Pioli et al., 2009; Rowland et al., 2009; Valentine et al., 2005). As an example, volumes of the tephra blanket, of the cone and of the lava flow of the 1943–1952 eruption of Parícutin (Mexico), which is considered as the typical violent Strombolian eruption, are  $6.4 \times 10^8$ ,  $2.5 \times 10^8$ , and  $7.0 \times 10^8$  m<sup>3</sup>, respectively (Fries, 1953; Pioli et al., 2008), which results in a volume fraction of the tephra blanket with respect to the total bulk volume of about 40%. The same volume fraction of 40% was reported for the 1759–1774 violent Strombolian eruption of El Jorullo (Mexico) with a volume of tephra blanket, cone, and lava flow of  $3.8 \times 10^8$ ,  $1.6 \times 10^8$ , and  $4.0 \times 10^8$  m<sup>3</sup>, respectively (Rowland et al., 2009). In contrast, the cumulative tephra blanket of the Tajogaite eruption is only 10% of the total eruptive volume (7%–16% if considering the variability of lava volume as shown in Figure 9), and in fact, LU1, LU, MU, UU, and the total deposit all plot within the field of decoupled systems even though the cumulative MER ( $5.4$ – $8.3 \times 10^4$  kg s<sup>-1</sup>; Table 4) is of the same order of violent Strombolian eruptions (Figure 10b). The layer LU1 is associated with the only phase of the eruption with an explosivity ratio (tephra blanket/total mass) > 0.1 (Figure 10b), which in fact corresponds to the phase with low emission rate of lava (Figures 5 and 9). Regardless of a similar cone height, more explosive basaltic eruptions are associated with larger volume fraction of tephra blanket versus total volume, such as the sub-Plinian eruption of Sunset crater with a total volume of tephra blanket, cone and lava flow of  $7.8 \times 10^8$ ,  $2.9 \times 10^8$ , and  $1.4 \times 10^8$  m<sup>3</sup>, respectively, resulting in a volume fraction of 64% (Alfano et al., 2018), and the Pleistocene Cerro Negro cone (Chile) where the tephra cone is associated with a bulk volume of 0.94 km<sup>3</sup>, while the lava is only 0.03 km<sup>3</sup> (in this case the volume of the tephra blanket could not be determined because of erosion) (Romero et al., 2022b).

It is important to bear in mind that, given that only subaerial lava is considered in our analysis, the total MER of the various layers and units and of the total eruption is expected to be larger, however, the explosivity parameters (mass of tephra blanket/total mass) are expected to be even lower. In fact, the uncertainty on the determination of the volume of lava (50% on the subaerial lava field + unknown fraction on the subaquatic lava flows) is impacting the final classification analysis more than the variability associated with the determination of volume of tephra (blanket and cone) and on the duration of the different eruptive phases (<30%) (Tables 2–4). Considering all known uncertainties, the Tajogaite eruption plots in the field of decoupling systems and long-lasting hybrid eruptions (Figures 8 and 10 and Figure S10 in Supporting Information S1). We conclude that, if the classification was only based on tephra, the Tajogaite eruption would classify as VEI 3. Nonetheless, when all the eruptive products are considered (tephra blanket, scoria cone, lava flow), the Tajogaite eruption can be better described as a long-lasting hybrid eruption associated with a decoupled magma-gas system that produced a large volume of degassed magma with only a small fraction resulting in efficient fragmentation (i.e., 7%–16% of tephra blanket versus total volume (tephra blanket, cone, lava) and 38% of tephra blanket versus total tephra volume (blanket, cone)).

## 6. Conclusions

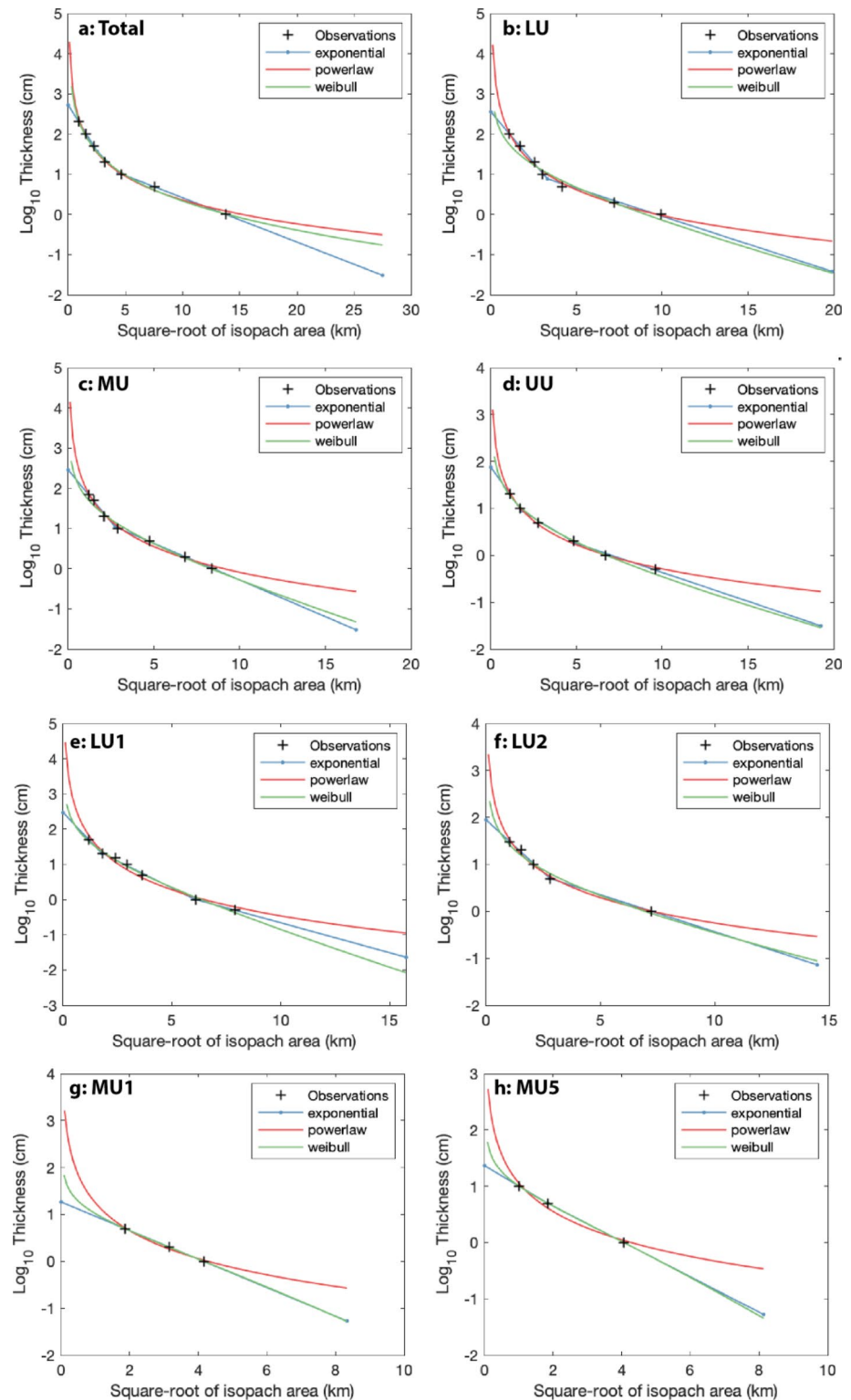
The nearly 3-month-long 2021 eruption of Cumbre Vieja (Tajogaite eruption) represents a long-lasting, hybrid eruption associated with multiple eruptive styles (effusive, lava fountains, ash emissions, Strombolian explosions) from multiple vents along a 0.5 km fissure and resulting in multiple eruptive products (lava flows, tephra cone, tephra blanket). Detailed field analysis of the tephra blanket during and after the eruption, in combination with

the analysis of atmospheric wind data, volcanic tremor, lava emission rates, and all associated uncertainties, provide key insights into the features and dynamic of the eruption:

1. The MER associated with the tephra blanket was relatively constant during the eruption ( $\sim 3\text{--}4 \times 10^3 \text{ kg s}^{-1}$ ). In contrast, the emission rate of lava oscillated through time (with the largest peak during LU2 after a major cone collapse), but always remained higher than the cumulative MER of tephra blanket and tephra cone (average value of lava emission rate of  $6.3 \pm 3.2 \times 10^4 \text{ kg s}^{-1}$ ).
2. Even though plume height is often taken as a proxy for the variation of MER, the daily variation of plume height during the Tajogaite eruption was more related to the impact of the wind on plume rise than to the short-term variation of MER; in fact, low and high plumes well correlate with the presence of strong (Type 1) or absent/weak (Type 2) trade winds, respectively.
3. Regardless of the complexity of eruptive styles and eruptive dynamics, the tephra blanket provides an excellent record of the whole eruption with distinct sublayers, layers, and units that can be well correlated at various distances from the vent and with both the recorded volcanic tremor and the emission rate of lava.
4. The whole tephra blanket, as well as individual units and most layers, are elongated NE-SW, except for MU1 layer, which is mostly dispersed to the SSW. This dispersal pattern is the result of the modulation of trade winds that control the dispersal to the SW when intense and can result in more complex wind patterns when weak or absent. The general wind pattern was also impacted by the daily land/sea breeze and the convection induced by the extended lava-flow field, all these aspects challenging the short-range operational ash dispersal forecasts.
5. The thinning trends provide a bulk volume of  $2.3 \pm 0.2 \times 10^7 \text{ m}^3$  for the whole tephra blanket, between  $4.5 \pm 0.8$  and  $9.2 \pm 0.6 \times 10^6 \text{ m}^3$  for the three units (LU, MU, UU) and between  $1.3 \pm 0.2$  and  $4.9 \pm 0.7 \times 10^6 \text{ m}^3$  for selected layers (LU1, LU2, MU1, MU5) (based on power law integration).
6. The populations of the 20 largest scoria clasts in the most proximal locations SW (LP35) and NE (LP27) of the vents show a similar grainsize, with the 50th percentile varying between 1.3 and 1.9 cm.
7. The Tajogaite eruption confirms the need of dedicated multidisciplinary strategies to characterize and classify long-lasting, hybrid eruptions that not only consider the tephra blanket (e.g., VEI, tephra blanket thinning), but also include the evolution of the tephra cone and the lava-flow field such as the plot of explosivity index (mass of tephra blanket versus total mass) and Magnitude Index versus Intensity Index plot. In fact, the tephra blanket only represents 7%–16% of the total bulk erupted volume of tephra blanket, tephra cone, and lava field ( $1\text{--}3 \times 10^8 \text{ m}^3$ ). Nonetheless, the tephra blanket of the Tajogaite eruption is key to decipher the variable eruptive dynamics through time.

Appendix A

Thinning trends of the tephra blankets used for the determination of erupted volume.



**Figure A1.** Thinning trends (exponential, power law, and Weibull) of the tephra blanket for (a) total deposit, (b) Lower Unit (LU), (c) Middle Unit (MU), (d) Upper Unit (UU), (e) LU1, (f) LU2, (g) MU1, and (h) MU5.

## Data Availability Statement

Data used in this manuscript are available in Tables 4 and Tables S1–S5 in Supporting Information S1 or are extracted from cited references (Andronico et al., 2014; Civico et al., 2022a, 2022b; Coltelli et al., 1998; Connor & Connor, 2006; Costantini et al., 2009; Freret-Lorgeril et al., 2021a, 2021b; Houghton et al., 2004; Moreno, 1980; Naranjo et al., 1991; Rose et al., 2008; Rowland et al., 2009; Scollo et al., 2013; Pioli et al., 2009; Pistolesi et al., 2011; Pyle, 2000; see captions of individual figures for more details on the use of these references). Plume height (PEVOLCA and VONA; Figure 2), volcanic tremor (Figure 5), deposit thinning (Figure 8), and lava emission (Figure 9) data can be found in Zenodo (<https://doi.org/10.5281/zenodo.7241538>). Lava flow outlines in Figure 1 come from Copernicus Emergency Management Service (© 2021 European Union), EMSR546 (<https://emergency.copernicus.eu/mapping/list-of-components/EMSR546>, last accessed 2022-07-29). The background DEM in Figures 1, 4, 6, and 7 is the 10-m Copernicus DEM (© 2021 European Union) (<https://spacedata.copernicus.eu/web/cscda/dataset-details?articleId=394198>, last accessed 2022-07-29). Software used to make figures include Microsoft Excel 365 (© Microsoft), Matlab v.2018b (MATLAB, 2018), Matplotlib v.3.5.2 (Caswell et al., 2022; Hunter, 2007), QGIS (QGIS Development Team, 2022), and Adobe Illustrator (© 2022 Adobe). Lava emission (Figure 9) was estimated using satellite thermal data processed by the MIROVA system which is based on the analysis of MODIS (Moderate Resolution Imaging Spectroradiometer) infrared data (Coppola et al., 2020). Ash dispersal modeling (Figure 11) was carried out with FALL3D dispersal model (Folch et al., 2020) available under the version 3 of the GNU General Public License (GPL) at <https://gitlab.com/fall3d-distribution>.

## Acknowledgments

Authors are grateful to the logistic support of the Instituto Volcanológico de Canarias (INVOLCAN) that was key to the development of this work with a special thanks to Matt Pankhurst and Nemesio Perez. Valentin Freret-Lorgeril, Allan Fries, Corine Frischknecht, Jonathan Lemus, and Eduardo Rossi (from the University of Geneva) are thanked for discussion and support in the field. Riccardo Civico, Tullio Ricci, Daniele Andronico, Jacopo Taddeuci, Piergiorgio Scarlato, and Elisabetta Del Bello (from Istituto Nazionale di Geofisica e Vulcanologia) are also thanked for discussion on various aspects of this work. The manuscript largely benefited from the constructive feedback of the Associate Editor and two anonymous reviewers. Research activities were supported by Swiss National Science Foundation (Grant 200020\_188757) and by the projects (a) VOLRISKMAC (MAC/3.5b/124) and (b) VOLRISKMAC II (MAC/2/3.5b/328), financed by the Program INTERREG VA Spain-Portugal MAC 2014–2020 of the European Commission; (c) Cumbre Vieja Emergencia, financed by the Science and Innovation Ministry, Spanish Government; and (d) Tfassistance, financed by the Cabildo Insular de Tenerife. JER fieldwork was partially financed through NSFGEONERC-DisEqm (NERC Reference: NE/N018575/1) and V-PLUS projects (Prof. Mike Burton). We also acknowledge the multiyear PRACE Project Access “Volcanic ash hazard and forecast” (ID 2019215114) and the Barcelona Supercomputing Center (BSC) for the allocation of supercomputing resources during the operational ash forecast.

## References

- Abdel-Monem, A., Watkins, N., & Gast, P. W. (1972). Potassium-argon ages, volcanic stratigraphy, and geomagnetic polarity history of the Canary Islands; Tenerife, La Palma. *American Journal of Science*, 272(9), 805–825. <https://doi.org/10.2475/ajs.272.9.805>
- Alfano, F., Bonadonna, C., Volentik, A. C. M., Connor, C. B., Watt, S. F. L., Pyle, D. M., et al. (2011). Tephra stratigraphy and eruptive volume of the May, 2008, Chaitén eruption, Chile. *Bulletin of Volcanology*, 73, 613–630. <https://doi.org/10.1007/s00445-010-0428-x>
- Alfano, F., Ort, M. H., Pioli, L., Self, S., Hanson, S. L., Roggensack, K., et al. (2018). Subplinian monogenetic basaltic eruption of Sunset Crater, Arizona, USA. *Geological Society of America Bulletin*, 131(3–4), 661–674. <https://doi.org/10.1130/B31905.1>
- Ancochea, E., Hernán, F., Cendrero, A., Cantagrel, J. M., Fúster, J., Ibarrola, E., & Coello, J. (1994). Constructive and destructive episodes in the building of a young oceanic island, La Palma, Canary Islands, and genesis of the Caldera de Taburiente. *Journal of Volcanology and Geothermal Research*, 60(3–4), 243–262. [https://doi.org/10.1016/0377-0273\(94\)90054-x](https://doi.org/10.1016/0377-0273(94)90054-x)
- Andronico, D., Scollo, S., & Cristaldi, A. (2015). Unexpected hazards from tephra fallout at Mt Etna: The 23 November 2013 lava fountain. *Journal of Volcanology and Geothermal Research*, 304, 118–125. <https://doi.org/10.1016/j.jvolgeores.2015.08.007>
- Andronico, D., Scollo, S., Cristaldi, A., & Lo Castro, M. D. (2014). Representativity of incompletely sampled fall deposits in estimating eruption source parameters: A test using the 12–13 January 2011 lava fountain deposit from Mt. Etna volcano, Italy. *Bulletin of Volcanology*, 76(10), 861. <https://doi.org/10.1007/s00445-014-0861-3>
- Bagheri, G., & Bonadonna, C. (2016). Aerodynamics of volcanic particles: Characterization of size, shape, and settling velocity. In S. Mackie, K. Cashman, H. Ricketts, A. Rust, & M. Watson (Eds.), *Volcanic ash* (1st ed., p. 316). Elsevier, ISBN: 9780081004050
- Barker, A. K., Troll, V. R., Carracedo, J. C., & Nicholls, P. A. (2015). The magma plumbing system for the 1971 Teneguía eruption on La Palma, Canary Islands. *Contributions to Mineralogy and Petrology*, 170(5–6), 54. <https://doi.org/10.1007/s00410-015-1207-7>
- Beckett, F. M., Witham, C. S., Leadbetter, S. J., Crocker, R., Webster, H. N., Hort, M. C., et al. (2020). Atmospheric dispersion modelling at the London VAAC: A review of developments since the 2010 Eyjafjallajökull Volcano Ash Cloud. *Atmosphere*, 11, 352. <https://doi.org/10.3390/atmos11040352>
- Biass, S., Bagheri, G., Aeberhard, W., & Bonadonna, C. (2014). Terror: Towards a better quantification of the uncertainty propagated during the characterization of tephra deposits. *Statistics in Volcanology*, 1(2), 1–27. <https://doi.org/10.5038/2163-338X.1.2>
- Biass, S., Bonadonna, C., di Traglia, F., Pistolesi, M., Rosi, M., & Lestuzzi, P. (2016). Probabilistic evaluation of the physical impact of future tephra fallout events for the Island of Vulcano, Italy. *Bulletin of Volcanology*, 78, 37. <https://doi.org/10.1007/s00445-016-1028-1>
- Biass, S., Bonadonna, C., & Houghton, B. F. (2019). A step-by-step evaluation of empirical methods to quantify eruption source parameters from tephra-fall deposits. *Journal of Applied Volcanology*, 8, 1. <https://doi.org/10.1186/s13617-018-0081-1>
- Bonadonna, C., Biass, S., & Costa, A. (2015). Physical characterization of explosive volcanic eruptions based on tephra deposits: Propagation of uncertainties and sensitivity analysis. *Journal of Volcanology and Geothermal Research*, 296, 80–100. <https://doi.org/10.1016/j.jvolgeores.2015.03.009>
- Bonadonna, C., Cioni, R., Costa, A., Druitt, T., Phillips, J., Pioli, L., et al. (2016). MeMoVolc report on classification and dynamics of volcanic explosive eruptions. *Bulletin of Volcanology*, 78, 84. <https://doi.org/10.1007/s00445-016-1071-y>
- Bonadonna, C., Cioni, R., Pistolesi, M., Connor, C. B., Scollo, S., Pioli, L., & Rosi, M. (2013). Determination of the largest clast sizes of tephra deposits for the characterization of explosive eruptions: A study of the IAVCEI commission on tephra hazard modelling. *Bulletin of Volcanology*, 75(1), 680. <https://doi.org/10.1007/s00445-012-0680-3>
- Bonadonna, C., & Costa, A. (2013). Plume height, volume and classification of volcanic eruptions based on the Weibull function. *Bulletin of Volcanology*, 75, 742. <https://doi.org/10.1007/s00445-013-0742-1>
- Bonadonna, C., & Houghton, B. F. (2005). Total grain size distribution and volume of tephra-fall deposits. *Bulletin of Volcanology*, 67, 441–456. <https://doi.org/10.1007/s00445-004-0386-2>
- Booth, B., & Walker, G. P. L. (1973). Ash deposits from the new explosion crater, Etna 1971. *Philosophical Transactions of the Royal Society of London*, 274, 147–151.
- Carracedo, J. C., Badiola, E. R., Guillou, H., deLa Nuez, J., & Pérez Torrado, F. J. (2001). Geology and volcanology of La Palma and El Hierro, Western Canaries. *Estudios Geológicos*, 57, 175–273. <https://doi.org/10.3989/egool.01575-6134>

- Carracedo, J. C., Day, S., Guillou, H., Rodríguez Badiola, E., Canas, J. A., & Pérez Torrado, F. J. (1998). Hotspot volcanism close to a passive continental margin: The Canary Islands. *Geological Magazine*, 135(5), 591–604. <https://doi.org/10.1017/S0016756898001447>
- Carracedo, J. C., Day, S. J., Guillou, H., & Gravelstock, P. (1999). Later stages of volcanic evolution of La Palma, Canary Islands: Rift evolution, giant landslides, and the genesis of the Caldera de Taburiente. *Bulletin of the Geological Society of America*, 111(5), 755–768. [https://doi.org/10.1130/0016-7606\(1999\)111<0755:isoveo>2.3.CO;2](https://doi.org/10.1130/0016-7606(1999)111<0755:isoveo>2.3.CO;2)
- Carracedo, J. C., Troll, V. R., Day, J. M. D., Geiger, H., Aulinas, M., Soler, V., et al. (2022). The 2021 eruption of the Cumbre Vieja volcanic ridge on La Palma, Canary Islands. *Geology Today*, 38, 94–107. <https://doi.org/10.1111/gto.12388>
- Carrillo, J., Guerra, J. C., Cuevas, E., & Barrancos, J. (2016). Characterization of the marine boundary layer and the trade-wind inversion over the sub-tropical North Atlantic. *Boundary-Layer Meteorology*, 158(2), 311–330. <https://doi.org/10.1007/s10546-015-0081-1>
- Casillas, R., de la Nuez, J., Fernández Rodríguez, C., Colmenero Navarro, J. R., Jourdan, F., Harangi, S., & Lukács, R. (2020). Edad de las rocas volcánicas submarinas y plutónicas del Complejo Basal de La Palma: Implicaciones en la evolución geológica temprana de la isla. *Geogaceta*, 67, 47–50.
- Cassidy, M., Manga, M., Cashman, K., & Bachmann, O. (2018). Controls on explosive-effusive volcanic eruption styles. *Nature Communications*, 9, 2839. <https://doi.org/10.1038/s41467-018-05293-3>
- Castro, J. M., & Feisel, Y. (2022). Eruption of ultralow-viscosity basanite magma at Cumbre Vieja, La Palma, Canary Islands. *Nature Communications*, 13, 3174. <https://doi.org/10.1038/s41467-022-30905-4>
- Castro, J. M., & Gardner, J. E. (2008). Did magma ascent rate control the explosive-effusive transition at the Inyo volcanic chain, California? *Geology*, 36, 279–282. <https://doi.org/10.1130/g24453a.1>
- Caswell, T. A., Droettboom, M., Lee, A., de Andrade, E. S., Hoffmann, T., Klymak, J., et al. (2022). Matplotlib/matplotlib: Rel: v3.5.2 (Version v3.5.2). Zenodo. <https://doi.org/10.5281/zenodo.6513224>
- Chouet, B., Saccorotti, G., Martini, M., Dawson, P., De Luca, G., Milana, G., & Scarpa, R. (1997). Source and path effects in the wave fields of tremor and explosions at Stromboli Volcano, Italy. *Journal of Geophysical Research*, 102(B7), 15129–15150. <https://doi.org/10.1029/97JB00953>
- Cioni, R., Bertagnini, A., Santacroce, R., & Andronico, D. (2008). Explosive activity and eruption scenarios at Somma-Vesuvius (Italy): Towards a new classification scheme. *Journal of Volcanology and Geothermal Research*, 178(3), 331–346. <https://doi.org/10.1016/j.jvolgeores.2008.04.024>
- Civico, R., Ricci, T., Scarlato, P., Taddeucci, J., Andronico, D., Del Bello, E., et al. (2022a). High-resolution digital surface model of the 2021 eruption deposit of Cumbre Vieja volcano, La Palma, Spain. *Scientific Data*, 9, 435. <https://doi.org/10.1038/s41597-022-01551-8>
- Civico, R., Ricci, T., Scarlato, P., Taddeucci, J., Andronico, D., Del Bello, E., et al. (2022b). 2021 Cumbre Vieja volcano eruption (La Palma, Spain) SfM DSM, Jan 2022. Distributed by *OpenTopography*. <https://doi.org/10.5069/G96971S8>
- Coltelli, M., Del Carlo, P., & Vezzoli, L. (1998). Discovery of a Plinian basaltic eruption of Roman age at Etna Volcano, Italy. *Geology*, 26, 1095–1098. [https://doi.org/10.1130/0091-7613\(1998\)026<1095:doapbe>2.3.co;2](https://doi.org/10.1130/0091-7613(1998)026<1095:doapbe>2.3.co;2)
- Connor, L. J., & Connor, C. B. (2006). Inversion is the key to dispersion: Understanding eruption dynamics by inverting tephra fallout. In H. M. Mader, S. G. Cole, C. B. Connor, & L. J. Connor (Eds.), *Statistics in volcanology. Special publications of IAVCEI* (pp. 231–242). Geological Society.
- Coppola, D., Barsotti, S., Cigolini, C., Laiolo, M., Pfeffer, M. A., & Ripepe, M. (2019). Monitoring the time-averaged discharge rates, volumes and emplacement style of large lava flows by using MIROVA system: The case of the 2014–2015 eruption at Holuhraun (Iceland). *Annals of Geophysics*, 61, VO221. <https://doi.org/10.4401/ag-7812>
- Coppola, D., Laiolo, M., Cigolini, C., Massimetti, F., Delle Donne, D., Ripepe, M., et al. (2020). Thermal remote sensing for global volcano monitoring: Experiences from the MIROVA system. *Frontiers of Earth Science*, 7, 362. <https://doi.org/10.3389/feart.2019.00362>
- Coppola, D., Laiolo, M., Piscopo, D., & Cigolini, C. (2013). Rheological control on the radiant density of active lava flows and domes. *Journal of Volcanology and Geothermal Research*, 249, 39–48. <https://doi.org/10.1016/j.jvolgeores.2012.09.005>
- Coppola, D., Valade, S., Masias, P., Laiolo, M., Massimetti, F., Campus, A., et al. (2022). Shallow magma convection evidenced by excess degassing and thermal radiation during the dome-forming Sabancaya eruption (2012–2020). *Bulletin of Volcanology*, 84, 16. <https://doi.org/10.1007/s00445-022-01523-1>
- Costantini, L., Bonadonna, C., Houghton, B. F., & Wehrmann, H. (2009). New physical characterization of the Fontana Lapilli basaltic Plinian eruption, Nicaragua. *Bulletin of Volcanology*, 71(3), 337–355. <https://doi.org/10.1007/s00445-008-0227-9>
- D'Auria, L., Koulakov, I., Prudencio, J., Cabrera-Perez, I., Ibanez, J., Martinez, J. B., et al. (2022). Voluminous storage and rapid magma ascent beneath La Palma revealed by seismic tomography. *Scientific Reports*, 1–4. <https://doi.org/10.21203/rs.3.rs-1238072/v1>
- D'Auria, L., & Martini, M. (2009). Slug flow: Modeling in a conduit and associated elastic radiation. In *Encyclopaedia of complexity and systems science*. Springer.
- Day, S. J., Carracedo, J. C., Guillou, H., & Gravelstock, P. (1999). Recent structural evolution of the Cumbre Vieja volcano, La Palma, Canary Islands: Volcanic rift zone reconfiguration as a precursor to volcano flank instability? *Journal of Volcanology and Geothermal Research*, 94(1–4), 135–167. [https://doi.org/10.1016/S0377-0273\(99\)00101-8](https://doi.org/10.1016/S0377-0273(99)00101-8)
- Degruyter, W., & Bonadonna, C. (2012). Improving on mass flow rate estimates of volcanic eruptions. *Geophysical Research Letters*, 39, L16308. <https://doi.org/10.1029/2012GL052566>
- Degruyter, W., & Bonadonna, C. (2013). Impact of wind on the condition for column collapse of volcanic plumes. *Earth and Planetary Science Letters*, 377–378, 218–226. <https://doi.org/10.1016/j.epsl.2013.06.041>
- Deligne, N. I., Horspool, N., Canessa, S., Matcham, I., Williams, G. T., Wilson, G., et al. (2017). Evaluating the impacts of volcanic eruptions using RiskScape. *Journal of Applied Volcanology*, 6, 18. <https://doi.org/10.1186/s13617-017-0069-2>
- Di Traglia, F. (2011). *The last 1000 years of eruptive activity at the Fossa cone (Island of Vulcano, Southern Italy)* (PhD thesis). University of Pisa.
- Dominguez, L., Pioli, L., Bonadonna, C., Connor, C. B., Andronico, D., Harris, A. J. L., & Ripepe, M. (2016). Quantifying unsteadiness and dynamics of pulsatory volcanic activity. *Earth and Planetary Science Letters*, 444, 160–168. <https://doi.org/10.1016/j.epsl.2016.03.048>
- Fearnley, C. J., & Beaven, S. (2018). Volcano alert level systems: Managing the challenges of effective volcanic crisis communication. *Bulletin of Volcanology*, 80, 46. <https://doi.org/10.1007/s00445-018-1219-2>
- Felpeo, A., Molina-Arias, A. J., Quirós, F., Pereda, J., García-Cañada, L., & Díaz-Suárez, E. A. (2022). Measuring the height of the eruptive column during the 2021 eruption of Cumbre Vieja (La Palma Island, Canary Islands). EGU General Assembly, Vienna, Austria 23–27 May 2022, EGU22-9419. <https://doi.org/10.5194/egusphere-egu22-9419>
- Fernández, J., Escayo, J., & Hu, Z. (2021). Detection of volcanic unrest onset in La Palma, Canary Islands, evolution and implications. *Scientific Reports*, 11, 2540. <https://doi.org/10.1038/s41598-021-82292-3>
- Folch, A. (2012). A review of tephra transport and dispersal models: Evolution, current status, and future perspectives. *Journal of Volcanology and Geothermal Research*, 235–236, 96–115. <https://doi.org/10.1016/j.jvolgeores.2012.05.020>

- Folch, A., Mingari, L., Gutierrez, N., Hanzich, M., Macedonio, G., & Costa, A. (2020). FALL3D-8.0: A computational model for atmospheric transport and deposition of particles, aerosols and radionuclides—Part I: Model physics and numerics. *Geoscientific Model Development*, *13*, 1431–1458. <https://doi.org/10.5194/gmd-13-1431-2020>
- Foshag, W. F., & González, J. (1956). Birth and development of Parícutin Volcano Mexico. *Bulletin of the United States Geological Survey*, *965*, 355–489.
- Freret-Lorgeril, V., Bonadonna, C., Corradini, S., Donnadieu, F., Guerrieri, L., Lacanna, G., et al. (2021a). Examples of multi-sensor determination of eruptive source parameters of explosive events at Mount Etna. *Remote Sensing*, *13*, 2097. <https://doi.org/10.3390/rs13112097>
- Freret-Lorgeril, V., Bonadonna, C., Corradini, S., Guerrieri, L., Lemus, J., Donnadieu, F. M., et al. (2021b). Tephra characterization and multi-disciplinary determination of eruptive source parameters of a weak paroxysm at Mount Etna (Italy). *Journal of Volcanology and Geothermal Research*, *421*, 107431. <https://doi.org/10.1016/j.jvolgeores.2021.107431>
- Freret-Lorgeril, V., Donnadieu, F., Scollo, S., Provost, A., Fréville, P., Guéhenneux, Y., et al. (2018). Mass eruption rates of tephra plumes during the 2011–2015 lava fountain paroxysms at Mt. Etna from Doppler radar retrievals. *Frontiers of Earth Science*, *6*, 73. <https://doi.org/10.3389/feart.2018.00073>
- Fries, C. J. (1953). Volumes and weights of pyroclastic material, lava, and water erupted by Parícutin Volcano, Michoacan, Mexico. *Transactions-American Geophysical Union*, *34*, 603–616. <https://doi.org/10.1029/tr034i004p00603>
- González, P. J. (2022). Volcano-tectonic control of Cumbre Vieja. *Science*, *375*(6587), 1348–1349. <https://doi.org/10.1126/science.abn5148>
- Hicks, A., & Few, R. (2015). Trajectories of social vulnerability during the Soufrière Hills volcanic crisis. *Journal of Applied Volcanology*, *4*, 10. <https://doi.org/10.1186/s13617-015-0029-7>
- Hill, B. E., Connor, C. B., Jarzempa, M. S., La Femina, P., Navarro, M., & Strauch, W. (1998). 1995 eruption of Cerro Negro Volcano, Nicaragua, and risk assessment for future eruptions. *The Geological Society of America Bulletin*, *110*, 1231–1241. [https://doi.org/10.1130/0016-7606\(1998\)110<1231:eocvvn>2.3.co;2](https://doi.org/10.1130/0016-7606(1998)110<1231:eocvvn>2.3.co;2)
- Houghton, B. F., Wilson, C. J. N., Del Carlo, P., Coltelli, M., Sable, J. E., & Carey, R. (2004). The influence of conduit processes on changes in style of basaltic Plinian eruptions: Tarawera 1886 and Etna 122 BC. *Journal of Volcanology and Geothermal Research*, *137*, 1–14. <https://doi.org/10.1016/j.jvolgeores.2004.05.009>
- Houghton, B. F., Wilson, C. J. N., & Pyle, D. M. (2000). Pyroclastic fall deposits. In H. Sigurdsson (Ed.), *Encyclopaedia of volcanoes* (pp. 555–570). Academic Press.
- Hunter, J. D. (2007). Matplotlib: A 2D graphics environment. *Computing in Science & Engineering*, *9*(3), 90–95. <https://doi.org/10.1109/mcse.2007.55>
- Iacovino, K., & Till, C. B. (2019). DensityX: A program for calculating the densities of magmatic liquids up to 1,627°C and 30 kbar. *Volcanica*, *2*(1), 1–10. <https://doi.org/10.30909/vol.02.01.0110>
- Irl, S. D. H., Harter, D. E. V., Steinbauer, M. J., Puyol, D. G., Fernández-Palacios, J. M., Jentsch, A., et al. (2015). Climate vs. topography—Spatial patterns of plant species diversity and endemism on a high-elevation island. *Journal of Ecology*, *103*, 1621–1633. <https://doi.org/10.1111/1365-2745.12463>
- Klawonn, M., Houghton, B. F., Swanson, D. A., Fagents, S. A., Wessel, P., & Wolfe, C. J. (2014). Constraining explosive volcanism: Subjective choices during estimates of eruption magnitude. *Bulletin of Volcanology*, *76*(2), 793. <https://doi.org/10.1007/s00445-013-0793-3>
- Klügel, A., Schmincke, H. U., White, J. D. L., & Hoernle, K. A. (1999). Chronology and volcanology of the 1949 multi-vent rift-zone eruption on La Palma (Canary Islands). *Journal of Volcanology and Geothermal Research*, *94*(1–4), 267–282. [https://doi.org/10.1016/S0377-0273\(99\)00107-9](https://doi.org/10.1016/S0377-0273(99)00107-9)
- Krauskopf, K. (1948). Mechanism of eruption at Parícutin Volcano, Mexico. *The Geological Society of America Bulletin*, *59*, 711–732. [https://doi.org/10.1130/0016-7606\(1948\)59\[711:moeapv\]2.0.co;2](https://doi.org/10.1130/0016-7606(1948)59[711:moeapv]2.0.co;2)
- Longpré, M.-A. (2021). Reactivation of Cumbre Vieja volcano. *Science*, *374*, 1197.
- Macdonald, G. A. (1972). *Volcanoes* (p. 510). Prentice-Hall.
- Mangan, M. T., & Cashman, K. V. (1996). The structure of basaltic scoria and reticulite and inferences for vesiculation, foam formation, and fragmentation in lava fountains. *Journal of Volcanology and Geothermal Research*, *73*, 1–18. [https://doi.org/10.1016/0377-0273\(96\)00018-2](https://doi.org/10.1016/0377-0273(96)00018-2)
- MATLAB. (2018). *Version 9.5 (R2018b)*. The MathWorks Inc.
- McGetchin, T. R., Settle, M., & Chouet, B. A. (1974). Cinder cone growth modelled after Northeast Crater, Mount Etna, Sicily. *Journal of Geophysical Research*, *79*(23), 3257–3272. <https://doi.org/10.1029/JB079i023p03257>
- Michaud-Dubuy, A., Carazzo, G., & Kaminski, E. (2020). Wind entrainment in jets with reversing buoyancy: Implications for volcanic plumes. *Journal of Geophysical Research: Solid Earth*, *125*, e2020JB020136. <https://doi.org/10.1029/2020JB020136>
- Moreno, H. (1980). La erupción del volcán Mirador en Abril-Mayo de 1979. In *Lago Ranco-Riñihue, Andes del Sur* (Vol. 28, pp. 1–23). Universidad de Chile, Departamento de Geología, Comunicaciones.
- Naranjo, J. A., Moreno, H., & Gardeweg, M. (1991). Erupción de 1988-1990 del volcán Lonquimay. In *Andes del Sur (38°20'S)* (Vol. 1, pp. 445–448). Actas VI Congreso Geológico Chileno.
- Newhall, C. G., & Self, S. (1982). The volcanic explosivity index (VEI): An estimate of explosive magnitude for historical volcanism. *Journal of Geophysical Research*, *87*(NC2), 1231–1238. <https://doi.org/10.1029/JC087iC02p01231>
- Ordoñez, E. (1945). *El volcán de Parícutin* (p. 138). Comisión Impulsora y Coordinadora de la Investigación Científica México.
- Pankhurst, M. J., Scarrow, J. H., Barbee, O. A., Hickey, J., Coldwell, B. C., Rollinson, G. K., et al. (2022). Rapid response petrology for the opening eruptive phase of the 2021 Cumbre Vieja eruption, La Palma, Canary Islands. *Volcanica*, *5*(1), 1–10. <https://doi.org/10.30909/vol.05.01.0110>
- Parfitt, E. A. (2004). A discussion of the mechanisms of explosive basaltic eruptions. *Journal of Volcanology and Geothermal Research*, *134*, 77–107. <https://doi.org/10.1016/j.jvolgeores.2004.01.002>
- Pioli, L., Azzopardi, B. J., & Cashman, K. V. (2009). Controls on the explosivity of scoria cone eruptions: Magma segregation at conduit junctions. *Journal of Volcanology and Geothermal Research*, *186*(3–4), 407–415. <https://doi.org/10.1016/j.jvolgeores.2009.07.014>
- Pioli, L., Erlund, E., Johnson, E., Cashman, K., Wallace, P., Rosi, M., & Delgado-Granados, H. (2008). Explosive dynamics of violent strombolian eruptions: The eruption of Parícutin volcano 1943–1952 (Mexico). *Earth and Planetary Science Letters*, *271*, 359–368. <https://doi.org/10.1016/j.epsl.2008.04.026>
- Pioli, L., Palmas, M., Behncke, B., De Beni, E., Cantarero, M., & Scollo, S. (2022). Quantifying strombolian activity at Etna Volcano. *Geosciences*, *12*, 163. <https://doi.org/10.3390/geosciences12040163>
- Pistolesi, M., Aravena, A., Costantini, L., Vigiani, C., Cioni, R., & Bonadonna, C. (2021). Explosive behavior of intermediate magmas: The example of Cotopaxi volcano (Ecuador). *Geochemistry, Geophysics, Geosystems*, *22*, e2021GC009991. <https://doi.org/10.1029/2021GC009991>

- Pistolesi, M., Delle Donne, D., Pioli, L., Rosi, M., & Ripepe, M. (2011). The 15 March 2007 explosive crisis at Stromboli volcano, Italy: Assessing physical parameters through a multidisciplinary approach. *Journal of Geophysical Research*, *116*, B12206. <https://doi.org/10.1029/2011JB008527>
- Pyle, D. M. (1989). The thickness, volume and grainsize of tephra fall deposits. *Bulletin of Volcanology*, *51*(1), 1–15. <https://doi.org/10.1007/BF01086757>
- Pyle, D. M. (2000). Sizes of volcanic eruptions. In H. Sigurdsson (Ed.), *Encyclopaedia of volcanoes* (pp. 263–269). Academic Press.
- QGIS Development Team. (2022). QGIS geographic information system (manual). Retrieved from <https://www.qgis.org>
- Rees, J. D. (1979). Effects on the eruption of Parícutin Volcano on landforms, vegetation, and human occupancy. In P. O. Sheets, & D. K. Grayson (Eds.), *Volcanic activity and human ecology* (pp. 249–292). Academic Press. <https://doi.org/10.1016/b978-0-12-639120-6.50014-5>
- Ripepe, M., Poggi, P., Braun, T., & Gordeev, E. (1996). Infrasonic waves and volcanic tremor at Stromboli. *Geophysical Research Letters*, *23*(2), 181–184. <https://doi.org/10.1029/95GL03662>
- Romero, J. E., Burton, M., Cáceres, F., Taddeucci, J., Civico, R., Ricci, T., et al. (2022a). The initial phase of the 2021 Cumbre Vieja ridge eruption (Canary Islands): Products and dynamics controlling edifice growth and collapse. *Journal of Volcanology and Geothermal Research*, *431*, 107642. <https://doi.org/10.1016/j.jvolgeores.2022.107642>
- Romero, J. E., Ureta, G., Fuentes, P., Corgne, A., Naranjo, J. A., Ramírez, C. F., et al. (2022b). The eruptive history and magma composition of Pleistocene Cerro Negro volcano (Northern Chile): Implications for the complex evolution of large monogenetic volcanoes. *Journal of Volcanology and Geothermal Research*, *429*, 107618. <https://doi.org/10.1016/j.jvolgeores.2022.107618>
- Romero, J. E., Vera, F., Polacci, M., Morgavi, D., Arzilli, F., Alam, M. A., et al. (2018). Tephra from the 3 March 2015 sustained column related to explosive lava fountain activity at Volcán Villarrica (Chile). *Frontiers of Earth Science*, *6*, 98. <https://doi.org/10.3389/feart.2018.00098>
- Rose, W. I., Self, S., Murrow, P. J., Bonadonna, C., Durant, A. J., & Ernst, G. G. J. (2008). Nature and significance of small volume fall deposits at composite volcanoes: Insights from the October 14, 1974 Fuego eruption, Guatemala. *Bulletin of Volcanology*, *70*, 1043–1067. <https://doi.org/10.1007/s00445-007-0187-5>
- Rowland, S. K., Jurado-Chichay, Z. J., Ernst, G., & Walker, G. P. L. (2009). Pyroclastic deposits and lava flows from the 1759–1774 eruption of El Jorullo, México: Aspects of ‘Violent Strombolian’ activity and comparison with Parícutin. *Studies in Volcanology: The Legacy of George Walker* (Vol. 2, pp. 105–128). IAVCEI, Special Publications.
- Schipper, C. I., Castro, J. M., Tuffen, H., James, M. R., & How, P. (2013). Shallow vent architecture during hybrid explosive-effusive activity at Cordón Caulle (Chile, 2011–12): Evidence from direct observations and pyroclast textures. *Journal of Volcanology and Geothermal Research*, *262*, 25–37. <https://doi.org/10.1016/j.jvolgeores.2013.06.005>
- Scollo, S., Coltelli, M., Bonadonna, C., & Del Carlo, P. (2013). Tephra hazard assessment at Mt. Etna (Italy). *Natural Hazards and Earth System Sciences*, *13*, 3221–3233. <https://doi.org/10.5194/nhess-13-3221-2013>
- Staudigel, H., Feraud, G., & Giannerini, G. (1986). The history of intrusive activity on the island of La Palma (Canary Islands). *Journal of Volcanology and Geothermal Research*, *27*(3–4), 299–322. [https://doi.org/10.1016/0377-0273\(86\)90018-1](https://doi.org/10.1016/0377-0273(86)90018-1)
- Sword-Daniels, V., Wilson, T. M., Sargeant, S., Rossetto, T., Twigg, J., Johnston, D. M., et al. (2013). Consequences of long-term volcanic activity for essential services in Montserrat: Challenges, adaptations and resilience. In G. Wadge, B. Voight, & R. Robertson (Eds.), *The eruption of Soufrière Hills Volcano, Montserrat from 2000 to 2010*. Geological Society.
- Torres-González, P. A., Luengo-Oroz, N., Lamolda, H., D’Alessandro, W., Albert, H., Iribarren, I., et al. (2020). Unrest signals after 46 years of quiescence at Cumbre Vieja, La Palma, Canary Islands. *Journal of Volcanology and Geothermal Research*, *392*, 106757. <https://doi.org/10.1016/j.jvolgeores.2019.106757>
- Valentine, G. A. (1998). Eruption column physics. In A. Freundt, & M. Rosi (Eds.), *From magma to tephra* (pp. 91–138). Elsevier. [https://doi.org/10.1016/s1871-644x\(01\)80005-x](https://doi.org/10.1016/s1871-644x(01)80005-x)
- Valentine, G. A., & Gregg, T. K. P. (2008). Continental basaltic volcanoes—Processes and problems. *Journal of Volcanology and Geothermal Research*, *177*(4), 857–873. <https://doi.org/10.1016/j.jvolgeores.2008.01.050>
- Valentine, G. A., Krier, D., Perry, F. V., & Heiken, G. (2005). Scoria cone construction mechanisms, Lathrop wells volcano, southern Nevada, USA. *Geology*, *33*, 629–632. <https://doi.org/10.1130/g21459ar.1>
- Velasco, A. H. (1945). *Estudio de las cenizas del volcán caídas en la ciudad de México* (pp. 139–145). El Parícutin, Estado de Michoacán.
- Wadsworth, F. B., Llewellyn, E. W., Farquharson, J. I., Gillies, J. K., Loisel, A., Frey, L., et al. (2022). Crowd-sourcing observations of volcanic eruptions during the 2021 Fagradalsfjall and Cumbre Vieja events. *Nature Communications*, *13*, 2611. <https://doi.org/10.1038/s41467-022-30333-4>
- Wadsworth, F. B., Llewellyn, E. W., Vasseur, J., Gardner, J. E., & Tuffen, H. (2020). Explosive-effusive volcanic eruption transitions caused by sintering. *Science Advances*, *6*, eaba7940. <https://doi.org/10.1126/sciadv.aba7940>
- Walker, G. P. L. (1973). Explosive volcanic eruptions—A new classification scheme. *Geologische Rundschau*, *62*, 431–446. <https://doi.org/10.1007/bf01840108>
- Walker, G. P. L. (1980). The Taupo pumice: Product of the most powerful known (ultra-Plinian) eruption? *Journal of Volcanology and Geothermal Research*, *8*, 69–94. [https://doi.org/10.1016/0377-0273\(80\)90008-6](https://doi.org/10.1016/0377-0273(80)90008-6)
- Wolfe, E. W., Neal, C. A., Banks, N. G., & Duggan, T. J. (1988). Geologic observations and chronology of eruptive events. In E. W. Wolfe (Ed.), *The Puu Oo eruption of Kilauea Volcano, Hawaii: Episodes 1 Through 20, January 3, 1983 Through June 8, 1984*. U.S. Geological Survey Professional Paper (Vol. 1453, pp. 1–99).
- Woodhouse, M. J., Hogg, A. J., Phillips, J. C., & Sparks, R. S. J. (2013). Interaction between volcanic plumes and wind during the 2010 Eyjafjallajökull eruption, Iceland. *Journal of Geophysical Research: Solid Earth*, *118*, 92–109. <https://doi.org/10.1029/2012JB009592>
- Zawacki, E. E., Clarke, A. B., Arrowsmith, J. R., Bonadonna, C., & Lynch, D. J. (2019). Tecolote volcano, Pinacate volcanic field (Sonora, Mexico): A case of highly explosive basaltic volcanism and shifting eruptive styles. *Journal of Volcanology and Geothermal Research*, *379*, 23–44. <https://doi.org/10.1016/j.jvolgeores.2019.04.011>
- Zuccaro, G., Cacace, F., Spence, R. J. S., & Baxter, P. J. (2008). Impact of explosive eruption scenarios at Vesuvius. *Journal of Volcanology and Geothermal Research*, *178*(3), 416–453. <https://doi.org/10.1016/j.jvolgeores.2008.01.005>